

# PHOTOMETRIC REDSHIFTS AND SELECTION OF HIGH REDSHIFT GALAXIES IN THE NTT AND HUBBLE DEEP FIELDS.

ADRIANO FONTANA

Osservatorio Astronomico di Roma, Via dell' Osservatorio 2, I-00040, Monteporzio, Italy

SANDRO D'ODORICO

ESO, Karl-Schwarzschildstr. 2, Garching bei München, D-85748

FRANCESCO POLI, EMANUELE GIALONGO

Osservatorio Astronomico di Roma, Via dell' Osservatorio 2, I-00040, Monteporzio, Italy

STEPHANE ARNOUTS

ESO, Karl-Schwarzschildstr. 2, Garching bei München, D-85748

STEFANO CRISTIANI

Space Telescope European Coordinating Facility, ESO, Karl-Schwarzschildstr. 2, Garching bei München, D-85748

ALAN MOORWOOD

ESO, Karl-Schwarzschildstr. 2, Garching bei München, D-85748

PAOLO SARACCO

Osservatorio Astronomico di Brera, 22055 Merate (LC) Italy

*Submitted to AJ*

## ABSTRACT

We present and compare in this paper new photometric redshift catalogs of the galaxies in three public fields: the NTT Deep Field, the HDF-N and the HDF-S. In the case of the NTT Deep Field, we present here a new photometric catalog, obtained by combining the existing BVrI and JKs with new deep U observations acquired with NTT-SUSI2, and which includes also the contiguous field centered on the  $z_{em} = 4.7$  quasar BR1202-07.

Photometric redshifts have been obtained for the whole sample (NTTDF + HDF-N + HDF-S), by adopting a  $\chi^2$  minimization technique on a spectral library drawn from the Bruzual and Charlot synthesis models, with the addition of dust and intergalactic absorption. The accuracy, determined from 125 galaxies with known spectroscopic redshifts, is  $\sigma_z \sim 0.08(0.3)$  in the redshift intervals  $z = 0 - 1.5(1.5 - 3.5)$ .

The global redshift distribution of I-selected galaxies shows a distinct peak at intermediate redshifts,  $z \simeq 0.6$  at  $I_{AB} \leq 26$  and  $z \simeq 0.8$  at  $I_{AB} \leq 27.5$  followed by a tail extending to  $z \simeq 6$ . Systematic differences exist among the fields, most notably the HDF-S which contains a much smaller number of galaxies at  $z \simeq 0.9$  and at  $z \geq 4.5$  than the HDF-N. We also present for the first time the redshift distribution of the total IR-selected sample to faint limits ( $Ks \leq 21$  and  $J \leq 22$ ). It is found that the number density of galaxies at  $1.25 < z < 1.5$  is  $\simeq 0.1 \text{ arcmin}^{-2}$  at  $J \leq 21$  and  $\simeq 1. \text{ arcmin}^{-2}$  at  $J \leq 22$ , and drops to  $\simeq 0.3 \text{ arcmin}^{-2}$  (at  $J \leq 22$ ) at  $1.5 < z < 2$ .

The HDFs data sets are used to compare the different results from color selection criteria and photometric redshifts in detecting galaxies in the redshift range  $3.5 \leq z \leq 4.5$ . Photometric redshifts predict a number of high  $z$  candidates in both the HDF-N and HDF-S that is nearly 2 times larger than color selection criteria, and it is shown that this is primarily due to the inclusion of dusty models that were discarded in the original color selection criteria by Madau et al 1998. In several cases, the selection of these objects is made possible by the additional constraints from the IR bands. This effect partially reflect the poor spectral sampling of the HDF filter set, and is not present in ground-based observations where a  $R - I \leq 0.5$  color selection criteria may be applied.

Finally, it is shown that galactic M stars may mimic  $z > 5$  candidates in the HDF filter set and that the 4 brightest candidates at  $z > 5$  in the HDF-S are indeed most likely M stars.

The data and photometric redshift catalogs presented here are available on line at <http://www.mporzio.astro.it/HIGHZ>.

*Subject headings:* galaxies: general – galaxies: photometry – methods: data analysis

## 1. INTRODUCTION

Starting with the pioneering studies of Kron (1980) and Tyson (1988), one of the main targets of deep imaging surveys has been the observation and study of galaxies at high redshift. The combination of deep imaging and systematic

spectroscopic follow-up has led to the discovery that the bulk of galaxies at the spectroscopic limit is made of blue star-forming galaxies at  $z \leq 1 - 1.5$ , where most of the stars of the present-day Universe appear to form (see Koo and Kron 1992, Ellis 1998 for extensive reviews).

A new approach recently developed to access the earlier

epochs of galaxy formation relies on deep multicolor surveys, where multiband images are taken with a complete set of standard broad-band filters in order to cover the overall spectrum of the galaxy and to discriminate the populations at different redshifts. In this case, the multiband catalogs are used to define sharp color criteria that select high redshift galaxy candidates (Steidel et al 1995, Madau et al 1996, Madau et al 1998, M98 hereafter, Fontana et al. 1996, Giallongo et al 1998, G98 hereafter). The very successful results of the spectroscopic follow-up of color selected samples (Steidel et al 1996, Steidel et al 1999) witness the reliability of the method.

However, this technique doesn't exploit all the information contained in multiband catalogs, that allow to sample the spectral shape of each galaxy over a very extended wavelength range. With this aim, the "photometric redshift" approach is rapidly becoming common practice. The concept that the redshift of a galaxy is reflected in its broad-band colors dates back to the early 60's (Baum 1962), and the existence of a definite relation between  $z$  and magnitude has been demonstrated by Koo (1985). However, extensive applications of this method have been developed only recently in order to analyze new sets of deep multicolor images. Following the original approach of Koo, methods have been applied to the HDF-N that make use of the observed redshift-magnitude relation (Connolly et al 1997, Wang et al 1998) derived from the spectroscopic subsample of the HDF-N. A different class of methods must be used when no large spectroscopic follow-up has been obtained yet, or when the technique is to be extended beyond the redshift range covered by the spectroscopic sample. In these cases, a spectral library is used to compute galaxy colors at any redshift, and a matching technique is used to obtain the best-fitting redshift. With different implementations, this method has been used on HDF-N (Sawicky 1997, Fernandez-Soto et al 1999, Benitez et al 1999, Arnouts et al 1999a) and ground-based data (G98, Fontana et al 1999a, Pello et al 1999).

Of paramount importance for the development of these applications have been the public surveys carried out over the last few years, primarily the HDF-N (Williams et al 1996) and HDF-S (Casertano et al 2000), since the superb photometric quality of the data and the extensive follow-up observations enable a large number of scientific issues to be addressed. Large ground-based telescopes have also been used to provide multicolor data with an extended wavelength coverage, often to support deep observations from space facilities. Examples are the VLT observations of the HDF-S-NICMOS field (Fontana et al 1999a) and the NTT observations of the whole HDF-S (Da Costa et al 1998) and of the AXAF Deep Field (Rengelink 1998). In this context, the field of the  $z = 4.7$  quasar BR1202-07 was one of the first where deep multicolor observations have been collected from ground to obtain catalogs suitable for determining photometric redshifts. First observations in the BVrI bands were used to search for galaxies at  $z \geq 4$  in the QSO surroundings, and led to the identification of a star-forming companion to the QSO (Fontana et al 1996, see also Hu et al 1996, Petitjean et al 1996, Fontana et al 1998), providing the first successful example of the "drop-out" technique at  $z \geq 4$ . From the same set of data, a photometric redshift distribution was obtained and discussed in G98. A much deeper field in the same

BVrI bands was obtained in 1997 with the SUSI1 imager at the NTT, and named "NTT Deep Field" (Arnout et al 1999b). Wider images covering both fields have been obtained in J and Ks during the commissioning phase of the SOFI infrared spectro-imager at the NTT (Saracco et al. 1999), and also made publicly available.

In this paper, we present new U band observations of the BR1202 and NTT Deep fields and describe the procedures used to produce the final UBvIJKs catalog in both fields (sect. 2). The photometric redshift technique is described in sect. 3 and applied to the NTT catalogs and to the public catalogs of the HDF-N and HDF-S. The main properties of the resulting photometric redshift catalogs are described in sect.4. In sect. 5, we focus on the selection of high redshift galaxies to discuss the differences of this approach with respect to the Lyman Lymit selection and the possible contamination by foreground M stars.

The photometric redshift catalogs presented here have been used to address several scientific issues in the high redshift Universe, ranging from the evolution of the luminosity density and the number of massive galaxies already assembled at early epochs (Fontana et al 1999b) to the evolution of galaxy sizes (Poli et al 1999, Giallongo et al 2000).

The data and photometric redshift catalogs are also available on line at the WEB site <http://www.mporzio.astro.it/HIGHZ>.

## 2. THE DATA

### 2.1. Observations and data reduction on the BR1202-07 fields

The new data used in this paper are deep UBvIJKs images taken with the ESO-NTT telescope on the field of the high redshift quasar BR1202-07 ( $z_{em} = 4.7$ ).

The B,V, Gunn  $r$  and I observations were taken with the NTT SUSI imager during two separate observing runs, on 23-26 Apr 1995 and during the spring of 1997 respectively. The pointings were chosen in order to obtain two slightly overlapping fields, with the first field (hereafter named BR1202) centered on the quasar and the second (NTT Deep Field, NTTDF hereafter) 100 arcsec south of it, resulting in a total field of  $2.3' \times 4.7'$ . Since observations were obtained with two slightly different instrumental setups, the two fields have been analyzed independently and the objects in the overlapping region have been used as a final test of the photometric catalog. The BVrI observations and data reduction of the BR1202 field are discussed in Fontana et al 1996 and G98. The NTTDF was observed in service mode by the NTT team in February through April 1997, and the data obtained are publicly available at <http://www.hq.eso.org/science/ndf>. Details of the observations, the data reduction and the photometric catalog are discussed in Arnouts et al 1999b. Image quality in both fields is quite good, with sub-arcsec seeing in all the final images. An image of the final field in the  $r$  band is shown in Fig 1.

The J and Ks observations were obtained with the SOFI spectro-imager at the ESO-NTT (Moorwood et al 1998a) in March 1998. The field of view of this instrument is considerably larger ( $5' \times 5'$ ) than the SUSI one so both fields could be observed simultaneously. The data reduction and calibration of the images are described in Saracco et al

1999 and publicly available at the ESO website.

We have extracted from the full format J and Ks frames two sub-images corresponding to the two SUSI fields described above, by locating a number of corresponding bright sources and applying a linear resampling to the images. Since this operation added a further rebin to the original pixels, altering the noise statistics, we estimated the final limiting magnitude of the IR images by computing the  $\sigma$ -clipped standard deviation of the intensity of the sky-background as measured in random positions of the rebinned image with a  $1''$  aperture (we have verified that the same procedure on the original image provides the same standard deviation). The resulting  $3\sigma$  limiting Johnson magnitudes are  $J \leq 23.4$  and  $Ks \leq 21.7$  respectively.

These data have been complemented with deep U images obtained with the new SUSI2 imager at ESO-NTT. This instrument is equipped with a mosaic of two  $4k \times 2k$  CCD chips with a field of view of  $5.5' \times 5.5'$  that matches the SOFI one. Observations were done with the same pointing as the SOFI observations, with the two former SUSI fields both falling on the same chip. Data were obtained during two clear nights on 21 and 24 April 1998. A total of 25200 second of integration time were obtained, split into individual exposures of 1200-1500 s each. Observations were done in dark sky under moderate seeing conditions (about  $1.4''$  on average). The instrument performance was somewhat reduced with respect to the nominal one because of residual parasitic light entering the detector, that produced an additional background pattern with an intensity of about 40% of the sky background in the U band. Several exposures of this scattered light were taken during a bad weather night (25 April 1998). The pattern proved to be constant and could therefore be subtracted from the individual raw images before further processing. Aside from this aspect, the data reduction followed the usual steps for deep images acquired in dither mode. It has been performed with the automated DITHER pipeline developed for the SUSI2 images at the Rome Observatory. It makes use of standard Midas commands and of SExtractor (Bertin and Arnouts 1998) to flat-field, align and coadd the images to produce a final image together with its absolute variance map (i.e. the variance in ADU of each pixel in the frame).

A set of spectrophotometric standard stars have been observed at several airmasses during both nights to calibrate the U images in the AB system. We estimate that the final accuracy of this procedure is of the order of 0.1 *mags*. Again, two smaller images rebinned and aligned to the BVrI frames were extracted, and their zeropoints were computed in order to match the U magnitude of the brightest objects.

For the reader's convenience, we summarize in Table 1 the main characteristics of these observations and compare them with those of the HDF-N and HDF-S, which cover similar areas and will also be used in the following sections.

## 2.2. The photometric catalogues in the BR1202 fields

Object detection and flux measurement have been performed with the SExtractor software. In the NTTDF we have repeated the procedure used in Arnouts et al 1999b by using the sum of the BVrI frames, that have compara-

ble seeing. The numbering, position and BVrI magnitudes of the NTTDF provided here are therefore identical to those published in Arnouts et al 1999b. In the case of the BR1202 field we have used the *r* image, that has the best seeing, to detect and deblend the objects, partly for consistency with G98 and partly because the addition of the BVI images - that have either worse seeing or less depth - did not result in an improved object detection. Since the aim of this work is to derive photometric redshifts of objects that are significantly above the detection threshold, the differences in the procedures adopted for object detection are not important, although they must be kept in mind when using the data. In particular, only the NTTDF has been used in Fontana et al 1999b to measure the evolution of the rest-frame UV luminosity density, using the I-selected sample. We have also performed an independent object detection on the Ks images alone to ensure that all the galaxies at  $Ks < 21$  were included in the catalogs. The only object detected in the IR images but not in the optical is the methane brown dwarfs already discussed in a separate paper (Cuby et al 1999).

We have first obtained a reference magnitude  $m_r$  in the *r* band for each object in both fields by obtaining both isophotal and aperture magnitudes in a  $2x$  FWHM aperture. The isophotal magnitude was used for the brighter objects, i.e. for those objects where the isophotal radius is larger than the aperture one. For fainter objects, an aperture correction to  $5''$  has been estimated on bright stars and applied to correct the  $2x$  FWHM aperture magnitude. Although this procedure is strictly valid for star-like objects only, it has been shown to be a good approximation for faint galaxies (Smail et al. 1995).

To obtain total magnitudes in the other bands we have first measured aperture magnitudes in a fixed circular area corresponding to  $2x$  FWHM of the detection frame. Total magnitudes in each band *i* have then been computed as  $m_i = m_i(2FWHM) - m_r(2FWHM) + m_r$ , i.e. the observed aperture colors with respect to the reference *r* band have been normalized to the total *r* magnitude  $m_r$  as obtained above. This procedure in principle ensures that colors - that are the quantities used in estimating the redshifts - are measured in the same physical region at any wavelength. In ground-based images this procedure is complicated by the different seeing of the images in the various bands. To compensate for this, we have degraded the *r* reference frame to the seeing of each band and computed the aperture colors  $m_i(2FWHM) - m_r(2FWHM)$  on the images with the same seeing. To give an idea of the importance of this effect, we have found roughly that each  $0.1''$  of difference in seeing translates to about a 0.1 *mags* difference in the aperture color, although the exact value depends obviously on the object morphology.

The zeropoints were corrected for galactic absorption assuming  $E(B - V) = 0.02$  (Burstein & Heiles 1982) with  $\delta U = 0.095$ ,  $\delta B = 0.084$ ,  $\delta V = 0.063$ ,  $\delta R = 0.05$ ,  $\delta I = 0.038$ . We summarize in Table 1 the zeropoints of the photometric systems adopted for the catalogs, namely AB for all the HDF catalogs and for the U band of the NTT fields, and Johnson for all the other bands of the NTT fields. Since we have not applied any color term to the Johnson magnitudes of the catalogs, the resulting magnitudes are calibrated in the "natural" system defined by our instrumental passbands (see Fontana et al 1996).

We have used the overlapping section of the two fields to compare the two photometric catalogs - that have been taken with slightly different instrumental setups and at different epochs. The differences found ( $\Delta B = +0.05$ ,  $\Delta V = -.135$ ,  $\Delta r = -0.05$ ,  $\Delta I = -.12$ ) are close to the limit of the quoted uncertainties on the zeropoints. Since the BR1202 field has been observed under more controlled photometric conditions, we have applied this set of small corrections to the NTTDF catalog to make the two catalogs fully consistent. However, the differences may be indicative of the actual uncertainties associated with the photometry on deep exposures from ground-based telescopes, that typically result from the stacking of several exposures obtained on different nights. We will discuss in Sect.3.2 the possible effects of these uncertainties on the photometric redshifts obtained.

The final catalogs produced (along with the photometric redshifts, see sect. 3) are reported in Table 2 and are available on line at <http://www.mporzio.astro.it/HIGHZ>. This table contains also the half-light radius measured with the morphological analysis described in Poli et al 1999.

### 2.3. The final galaxy samples

To produce the final catalogs on which photometric redshifts are computed, we have identified and removed from the final galaxy sample obvious bright stars using the CLASS\_STAR parameter provided by SExtractor. A threshold CLASS\_STAR < 0.9 has been set (at  $\leq 24$  in the NTTDF and  $\leq 23.5$  in the BR1202 field), on the basis of the comparison between ground-based and HST data (Arnouts et al 1999b). We have also made use of the more detailed morphological analysis by Poli et al (1999) to identify stars down to  $I = 24.5$  on the NTTDF only.

We have applied our photometric redshift code also to the HDF-N and HDF-S with the IR observations obtained at Kitt Peak (Dickinson 1998) and at NTT-SOFI (Da Costa et al, 1998), respectively. For the HDF-N we have used the multicolor catalog published by Fernandez-Soto et al (1999), which uses an optimal technique to match the optical and IR images that have a quite different seeing. A similar catalog for the HDF-S has been provided by the same authors and is available at the Stony Brook WEB site <http://www.ess.sunysb.edu/astro/hfds/home.html>. The Stony Brook catalog of the HDF-S contains also the NTT optical magnitudes (UBVRI) for each object, obtained from the public data of the EIS deep survey. Very little difference on the photometric redshift is found when the NTT data are used or not, which is due to the lower statistical weight (compared to WFPC data) that is associated with them. For this reason, we have used only WFPC bands in the optical and NTT-SOFI in the IR, for consistency with the HDF-N. In both cases we have clipped the outer regions of the frame with lower S/N. Obvious stars have been excluded at  $I_{AB} \leq 25.5$  in the HDF-S again on the basis of the SExtractor CLASS\_STAR < 0.9 morphological classification.

Also the complete set of HDF photometric redshift catalogs is available at <http://www.mporzio.astro.it/HIGHZ>

## 3. PHOTOMETRIC REDSHIFTS

### 3.1. The technique

Much emphasis has been recently placed on the choice of the spectral library used to compute galaxy colors as a function of redshift. Several authors (e.g. Fernandez-Soto et al 1999, Benitez 1999) use observed spectral templates (e.g. Coleman et al 1980). This has the obvious advantage of only relying on a compact set of empirically determined data, but these must be extended in the UV and IR regions using synthetic models and augmented with bluer templates to represent the vast fraction of blue galaxies that dominate the counts at faint magnitudes. An even more empirical approach is to determine a set of auto-functions from the spectroscopic control sample (Csabai et al 2000), from which a set of template spectra can be derived.

Our recipe for photometric redshifts is based on the use of spectral synthesis models, at present the GISSSEL library by Bruzual & Charlot. At the cost of an additional computational effort, these models allow - at least in principle - to take into account the spectral evolution of galaxies at high redshift. We will show below that these models are able to provide a redshift accuracy which is at least equivalent to more empirical choices. However, the main reason for following this approach is the gain in physical information on the properties of high redshift galaxies that can be obtained by comparing their observed spectral energy distributions with the model predictions. From the input parameters used to draw the best fitting solution for each galaxy we can indeed obtain estimates of the main physical quantities of each galaxy in the sample: age of the last major starburst, mass already assembled in stars and dust content. Even taking into account the known degeneracies among some of the input parameters, one may use this information in a statistical way to further constrain galaxy evolution. Applications of this technique have already been presented in G98 and we refer to forthcoming papers for further applications of this method.

In practice, we have used a Miller-Scalo initial mass function (IMF) including stars in the  $0.1 < M < 65 M_{\odot}$  range (the effect of different choices of the IMF has been shown in G98). We have considered the cases of metallicity  $Z = Z_{\odot}$ ,  $Z = 0.2Z_{\odot}$  and as low as  $Z = 0.02Z_{\odot}$  with a weak correlation between age and metallicity. For these models, we span over a grid of  $e$  - folding star formation time-scales  $\tau$  (from 0.3 Gyrs to constant) and ages to produce the evolution of different spectral types (the complete grid adopted is listed in G98). Since we are aware that the smoothly declining star-formation histories that we have used are a simplified rendition of the actual histories experienced by real galaxies, we have added a few models with additional bursts of star formation. In practice, we have overlaid short-lived burst (0.3 Gyr of timescale) to two evolving models (0.3 and 5 Gyr of timescale), starting at an age of 3 Gyr. In each model, we let a substantial fraction of the final mass in the galaxy to be assembled during the burst: 10%, 30% or 50% in the former and 10%, 20% or 30% in the latter (for higher fractions the light from the starburst would dominate that from the underlying galaxy at any wavelength). *A posteriori*, we have verified that "multiple burst" models account for about 16% of the best-fitting models. In 30% of them, removing the multiple bursts from the library changes the best fit by more than  $\Delta z = 0.05$ , and in 14 % of the cases by more than  $\Delta z = 0.2$ , but always less than  $\Delta z = 0.5$ . In

all these cases the burst models are selected to match the contemporary presence of a flat star-forming UV continuum and a large 4000Å break with a significant slope of the IR continuum, that is difficult to match with the simple exponential laws (see also the discussion on the Scalo  $b$  parameter in G98). Although the spectroscopic sample is too small to provide a meaningful statistics, we note that a marginal improvement of the photometric redshift accuracy is usually obtained with the “multiple burst” models. More important is the effect that these models have on the parameters estimated for the best fitting spectrum. For instance, the stellar mass in each galaxy is found lower by typically 20% (but up to 60%) at fixed redshift, because of the contribution of post-AGB stars (that have a low M/L) to the near-IR flux.

We have also added to all spectral synthesis model the reddening produced by internal dust (SMC, Pei 1992 and Calzetti, 1997) and Lyman series absorption produced by the intergalactic medium (Madau 1995). As a further improvement with respect to G98, we have added [OII] and H $\alpha$  emission lines by inverting the Kennicutt 1994 relations for the relevant IMF. The Ly $\alpha$  emission is less straightforward to implement, since the spectral properties at the Ly $\alpha$  frequency observed in spectroscopic samples range from strong emission lines to damped absorption systems. As a tradeoff, we have removed from the unattenuated spectrum the stellar absorption features at the Ly $\alpha$  frequency.

At any redshift, galaxies are allowed to have any age smaller than the Hubble time at that redshift ( $\Omega = 1$  and  $H_0 = 50 \text{ km s}^{-1} \text{ Mpc}^{-1}$  have been adopted throughout the paper). The choice of the cosmological parameters are not important, since only colors are effectively used in deriving the photometric redshifts.

From the large dataset ( $\simeq 5 \times 10^5$ ) of “simulated galaxies” thus produced we compute the expected fluxes  $F_{template,i}$  in any filter  $i$  by convolving the theoretical spectrum with the normalized transmission curve of the telescope+detector+filter system (see Pickles 1998 for the formulae adopted).

Finally, a  $\chi^2$ -minimization procedure has been applied to find the best-fitting spectral template to the observed fluxes. For each template  $t$  at any redshift  $z$  we first minimize

$$\chi_{t,z}^2 = \sum_i \left[ \frac{F_{observed,i} - s \cdot F_{template,i}}{\sigma_i} \right]^2 \quad (1)$$

with respect to the scaling factor  $s$  where  $F_{observed,i}$  is the flux observed in a given filter  $i$ ,  $\sigma_i$  is its uncertainty and the sum is over the filters used, and then we identify the best-fitting solution with the lowest  $\chi_{t,z}^2$ . The scaling factor  $s$  is applied to the input parameters of the input spectrum to compute all the rest-frame quantities, such as absolute magnitudes or stellar masses. The Stony Brook catalogs of the HDF-N and HDF-S provide  $F_{observed,i}$  and  $\sigma_i$  already in physical units (Jy), and are therefore directly usable in Eq. 1. In the two NTT fields, where catalogs are given in standard magnitudes  $m_i$  (zeropointed to the Johnson system),  $F_{observed,i}$  is given by  $F_{observed,i} = 10^{-0.4 \times (m_i - 48.59 - C_i)}$ , where  $C_i$  is the conversion factor from the AB to the Johnson systems, found by convolving an A0V stellar spectrum of the Pickles 1998

library with the telescope+detector+filter efficiency.

As is well known, the conversion between fluxes and magnitude is not well behaved as the noise level is approached, which raises the question of how non-detections are handled in Eq. 1. In the cases of the two HDFs, the Stony Brook catalogs provides very small or even negative fluxes for objects that are non detected (like “U-dropout” or faint galaxies with no IR detection), so that Eq. 1 can be directly applied. In the NTT fields, we have followed the common practice of defining a magnitude limit at a given  $\sigma$  level, and computed  $\chi_{t,z}^2$  according to the following recipe: *a*) we have discarded from the sum in Eq.1 the bandpasses where *both* the observed galaxy flux and the models fall below the limiting magnitude; *b*) we have included in the sum the bandpasses where the models lay above the limit: to weight properly the non-detection, the object has assigned zero flux and noise equal to the  $1\sigma$  magnitude limit.

The former approach is closer to the physical definition of “measure” and statistically cleaner, but relies on an accurate estimate of the noise level at very low fluxes, which in real images may be dominated by non-poissonian effects (such as residuals of flat-fielding, pixel correlation and accuracy of sky-subtraction) that may be difficult to quantify. The latter may be useful either on public data with conventional formats or when conservative upper limits on fluxes are more appropriate to the data available. It is therefore interesting to investigate the effects of the different criteria on the final photometric redshifts. To this purpose, we have converted the Stony Brook HDF-N catalog into magnitudes, and defined the  $1\sigma$  limits in the various bands by locating the magnitude at which  $\Delta m \simeq 1.08$ . We compare the photometric redshifts obtained in the original “flux” format and in the conventional “magnitude” one in Fig 2, differentiating galaxies in the three samples used in Fontana et al 1999b:  $K \leq 21$ ,  $I_{AB} \leq 26$ ,  $I_{AB} \leq 27.5$  It is seen that very modest differences arise only in the faintest sample, with a few galaxies migrating from  $z \simeq 0.5$  to  $z = 3 - 4$  and even less in the opposite way (which makes the choice of the “flux” format more conservative), and with some scatter in the  $z = 1 - 2$  region, where the different treatment of the IR band plays a role.

### 3.2. Comparison with spectroscopic samples

This procedure has been tested on a sample of 125 galaxies with spectroscopic redshifts and multicolor photometry. Of these, 112 come from the Cohen et al (2000) compilation of the HDF-N (we have included only objects that fall in the inner region of the frame, as for the whole optical catalog, see Sect. 2.3), 3 are taken from the Stony Brook public catalogs of the HDF-S, while the remaining 10 are taken from the VLT spectroscopic follow-up of “dropout” galaxies in the HDF-S and AXAF deep fields (Cristiani et al 2000). The results are shown in fig. 3, where we differentiate between objects with secure or uncertain redshift, following the classification by Cohen et al (2000).

If we consider only the objects with secure redshift, and remove the object at  $z \simeq 2.9$  with  $z_{phot} \simeq 0.2$ , for a total 101 objects, the accuracy is  $\sigma_z \simeq 0.08$  at  $0 < z < 1.5$  and  $\sigma_z \simeq 0.3$  at  $z > 2$ , that we keep as reference value. If we take all the galaxies in the sample, and remove only the three objects with clearly discrepant redshift, the accuracy

raise to  $\sigma_z \simeq 0.1$  at  $0 < z < 1.5$  and  $\sigma_z \simeq 0.32$  at  $z > 2$ . If we compute a 3-sigma clipped rms we obtain an accuracy  $\Delta z = 0.09$  over the whole redshift range, with 111 objects out of 125 (i.e. 89%), and  $\Delta z = 0.07$  in the  $0 < z < 1.5$  interval (85 objects out of 91, i.e. 93%). In any case, the relative precision  $\sigma[(z_{phot} - z_{spec})/(1 + z_{spec})]$  is always of the order of 0.05 in the  $z < 1.5$  sample, as in most of similar analysis (Cohen et al 2000).

A 5% systematic underestimate  $\langle \Delta z \rangle \simeq -0.14$  appears to exist at  $z > 2$  in the spectroscopic sample, similar to that found by a recent revised version of the photometric redshifts based on the Coleman spectra ( $\langle \Delta z \rangle \simeq 0.15$ , Lanzetta 2000), but with opposite sign.

We will explore in future works how this underestimate can be reduced with a different choice of the GISSEL grid. In particular, we are collecting a much wider spectroscopic sample in different fields (D’Odorico et al, in preparation, and within the “K20 project”, P.I. Cimatti) and with a variety of bandwidths to perform a more accurate calibration of the spectral library, especially in the range  $2 < z < 4$ , where most of the observed data come from the rest-frame UV spectra.

Undoubtedly, the availability of only one major spectroscopic control sample (the HDF-N) is a major limitation that prevents to some extent a full evaluation of all the systematics involved in photometric redshifts.

It is worth reminding that at least 4 different ingredients are needed to pin down an accurate recipe for photometric redshifts: i) the photometric catalog (which depends on the accuracy of data processing and calibration and on the procedure used to measure colors); ii) the knowledge of the response curve of the telescope+filters+detector system; iii) the spectral library used and iv) the matching algorithm used. Despite this, most of the current debate is focused on the best choice of the spectral library and the relative influence of the different components in a typical survey is far from being assessed, especially in the case of ground-based observations.

Some hints on the expected biases may be obtained by Monte Carlo simulations. However, these typically assume errors to be Gaussian distributed which may be an oversimplification since, at the very bright and very faint limits, the uncertainties involved in background estimation and flat-fielding may dominate the errors. In Fernandez-Soto et al 1999 and in Arnouts et al 1999a Monte Carlo simulations have been used to show that photometric redshifts in the HDF-N catalogs are stable with respect to noise fluctuation down to about  $I_{F814W} \simeq 28.5$ . Arnouts et al 1999a showed that the maximum number of misidentifications (i.e. shift in  $z$  exceeding 0.5) is below 30% in the  $I_{F814W} \simeq 28.5$  catalogs. We adopt here a brighter limit  $I_{F814W} \leq 27.5$  (much brighter than the  $I_{F814W}$  limiting magnitude), that is ultimately set by the depth of the bluest images ( $U_{F300W}$ ), so that a minimum  $(U-I)_{AB} \geq 1$  is still measurable. At this magnitude the misidentification are obviously much lower (see fig 4 of Arnouts et al 1999a). By analogy, we set an upper limit to  $I_{AB} \leq 26$  in the NTTDF.

As a first test of the effect of systematic differences, we have compared the photometric redshifts obtained in the NTTDF with the two different photometric calibrations (see Sect. 2.2). Fig. 4 (upper panel) shows the histogram

of the scatter between the photometric redshifts  $z'_{phot}$  obtained with the “original” calibration and the photometric redshifts  $z_{phot}$  resulting with the adopted calibration. We first note that, for most of the objects, the difference found is within the expected accuracy of photometric redshifts. Objects with clearly discrepant redshifts are typically faint and amount to only  $\simeq 3\%$  of the total, a result that is consistent with the Monte Carlo simulation of Arnouts et al 1999a, when scaled do the depth of the NTTDF. A close scrutiny of the  $z'_{phot} - z_{phot}$  relation (fig. 4, lower panel) shows that the systematic changes to the zeropoints induce systematic offsets in the photometric redshifts that vary with redshift as the spectral breaks pass across the various filters. These changes marginally affect the selection of high redshift galaxies in the NTTDF: two objects at  $z \simeq 2.8$  in the final catalog are assigned at  $z' \simeq 0.5$  with the original calibration (out of 40 in the  $2.5 < z < 3.5$  bin), compensated by two objects that are moved from  $z' \simeq 2.8$  to much lower  $z$ . One galaxy (out of 14) is added to the  $3.5 < z < 4.5$  bin with the adopted calibration. The major statistical effect is due to 5 objects that move from  $z' \simeq 2.3$  to  $z \simeq 2.6$ , slightly changing the predicted values in the UV luminosity density in the bins adopted in Fontana et al 1999b.

In the long run, we expect that extended spectroscopic follow-up of multicolor deep fields with different filter sets and in different regions of the sky will allow a detailed evaluation of the different systematics involved.

#### 4. REDSHIFT DISTRIBUTIONS

We discuss in this section the fundamental properties of the redshift distributions in the catalogs. Beyond being the basis for several scientific studies - as discussed in the introduction - these distributions can be used to compare the predictions of photometric redshift analyses in different fields and with different instrumental setups. Given the limited size of the fields (the HDFs and the NTTDF have areas of 4-4.8 arcmin<sup>2</sup>, respectively) small scale fluctuations are expected to lead to discrepancies in the redshift distributions. At the same time, photometric redshifts may still be regarded as an experimental technique and small uncertainties in the photometric calibration or inadequacy of the spectral templates in the different filter sets may also lead to small but systematic effects in the resulting redshifts. At the present stage, it is not possible to fully disentangle these effects, pending full spectroscopic follow-ups and independent checks of the image calibrations. However, the comparison among the results in different fields may be regarded as an estimate of the total uncertainties in this kind of analysis. For an evaluation of its effects on some scientific topics see Fontana et al 1999b.

Fig 5 shows the redshift distribution in the catalogs of the two fields around BR1202-07, separately (we remind the reader that these catalogs have different depths). The distribution of Fig 5b of the BR1202 field is similar to the one published in Giallongo et al 98, where no U and J band and poorer K data were available. We find here the typical characteristics of redshift distributions at faint limits i.e most of the galaxies are located at  $0.5 < z < 1$  with a tail extending to greater  $z$ .

Although the comparison between the  $r$ -selected distri-

bution of the BR1202 field and the I-selected distribution of the NTTDF is not straightforward, we note that the tail of high redshift galaxies is - as expected - more pronounced in the deeper sample. We also note that the position of the peak in the redshift distribution that is skewed to lower redshifts in the NTTDF compared to the BR1202 field, opposite to what is naively expected in a deeper sample. This is, however, consistent with the observed number densities in the two fields - the NTTDF being richer in relatively bright galaxies - and emphasizes the need for much wider surveys.

The average redshift distributions at faint limits can be obtained by merging the NTTDF and the two HDFs. Fig 6. shows the I-limited distributions, at  $I_{AB} \leq 26$  (for a total of 973 objects), resulting from the combination of NTTDF and the two HDFs, and at  $I_{AB} \leq 27.5$  (1361 objects), from the two HDFs alone.

The global redshift distribution shows again the well known features of a distinct peak at intermediate redshifts,  $z \simeq 0.6$  for the brighter and  $z \simeq 0.8$  for the fainter followed by a tail extending to the highest redshifts compatible with the I selection criteria.

A close scrutiny of the individual distributions reveals systematic differences amongst the fields. At both magnitude limits, the HDF-S has a much smaller number of galaxies at  $z \simeq 0.9$  than the HDF-N. Since the filter set used in both observations is identical, this effect is not likely to be an artefact of the photometric redshifts.

Finally, we use the combined data sets of NTTDF and HDFs to build the redshift distribution in IR selected samples shown in Fig 7. The basic scientific output of these distributions has been discussed in Fontana et al 1999b, where it is shown that the redshift distribution of K-band selected galaxies provides a direct estimate of the number of massive galaxies already assembled at high redshift. We provide here a more detailed view of the redshift distribution in J and K-selected samples at different magnitude limits. These distributions may be useful for tuning extended spectroscopic surveys with the new IR spectrographs that are being implemented at 8-m telescopes. These surveys are designed to improve the knowledge of the large scale structures and emission line features of galaxies in the range  $1 < z < 2$ , where spectroscopic measurements with optical spectrographs are difficult because of the lack of suitable features. We detail the observed number densities at different J and Ks limits in Table 3. We find that the number density of galaxies at  $1. < z < 1.5$  is  $\simeq 1 \text{ arcmin}^{-2}$  at  $J \leq 21$  and  $\simeq 3.8 \text{ arcmin}^{-2}$  at  $J \leq 22$ , and drops to  $\simeq 0.3 \text{ arcmin}^{-2}$  (at  $J \leq 22$ ) at  $1.5 < z < 2$ .

## 5. THE SELECTION OF HIGH REDSHIFT GALAXIES

### 5.1. Galaxies at $3.5 < z < 4.5$

The search for extremely high redshift galaxies is one of the most interesting applications of deep multicolor imaging. The so-called “dropout” technique has gained widespread popularity due to its simplicity and high success rate in detecting galaxies at  $z \geq 2.8$ . However, it is worth remembering that this method relies on the contemporary presence of *two* distinct features: the sharp cutoff provided by the intrinsic Lyman Limit (at  $z \leq 3.5$ ) or by the IGM Lyman $\alpha$  absorption (at higher  $z$ ) and the flat star-forming continuum at longer wavelengths, that

samples the rest-frame extreme UV spectral region. The latter criterium is necessary to discriminate against interlopers (e.g. intermediate  $z$  elliptical or dusty galaxies, or even late-type stars) that may also show a dramatic drop in their rest-frame near UV. In a nutshell, high redshift galaxies appear as objects that are “blue in the red and red in the blue”. An important consequence of this approach is that the “dropout” technique is essentially a highly conservative technique that is designed to minimize the fraction of interlopers, but that is biased against even moderately dust-reddened galaxies: as shown in Pettini et al 1997, even a relatively weak dust absorption ( $E(B - V) \simeq 0.15$  with an SMC extinction law) would prevent the detection of galaxies at  $z > 3$  in their well-studied *UGR* color plane.

Given the strength of the IGM color feature, color selection criteria and photometric redshifts provide comparable results when the filter set ensures an appropriate coverage of both features. This is illustrated at  $z \simeq 3$  in the VLT observations of the HDFs NICMOS field (Fontana et al 1999a) and at higher  $z$  in the previous version of the BR1202 catalog (G98), where a  $r - I \leq 0.2$  requirement was explicitly chosen to detect galaxies at  $4 \leq z \leq 4.5$ . A similar requirement  $R - I \leq 0.6$  has been adopted by Steidel et al 1999 to improve the rejection of low  $z$  interlopers in their first systematic spectroscopic follow up of  $z \geq 4$  candidates.

Unfortunately, a similar agreement between photometric redshifts and color selection criteria does not hold in the case of galaxies at  $3.5 \leq z \leq 4.5$  in the HDF-N and HDF-S. As a result, the estimate of the UV luminosity density obtained with color selection criteria ( $\phi_{1500} \simeq 5.0 \times 10^{25} \text{ erg s}^{-1} \text{ Hz}^{-1} \text{ Mpc}^{-3}$ , M98) is significantly different from that obtained with photometric redshifts ( $\phi_{1500} \simeq 10^{26} \text{ erg s}^{-1} \text{ Hz}^{-1} \text{ Mpc}^{-3}$ , Pascarella et al 1998, Fontana et al 1999b). This is primarily due to the much larger number of candidates selected by the latter technique (roughly 2 times larger). This difference appears rather puzzling at first glance, because both methods have been applied to the same data set (albeit on different catalogs) and the M98 selection criterium has been defined using a synthesis spectral library similar to the one used here.

To investigate the origin of this discrepancy, we reproduce in fig 8 the  $B_{450} - V_{606}$  vs  $V_{606} - I_{814}$  plane adopted by M98, whose selection criteria requires galaxy candidates to fall within the polygonal region shown in fig 8 (solid line), and to have  $V_{606} \leq 27.7$ . The latter requirement ensures a proper detection of the “B-dropout” and is therefore ultimately set by the depth of the  $B_{450}$  frame. We also plot in fig 8 the observed galaxy colors of the joined HDF-N + HDF-S catalogs, differentiating galaxies at different photometric redshifts. At variance with the M98 catalog, our data are limited at  $I_{814} \leq 27.5$ , that corresponds to a rest-frame wavelength of  $\simeq 1600 \text{ \AA}$ .

The following conclusions result from this comparison:

- Most of the galaxies lying within the M98 polygonal region have a photometric redshift falling in the  $3.5 \leq z \leq 4.5$  range. The few exception are in any case at  $z \geq 3.3$ , in agreement with the expected scatter of photometric redshifts. This confirms our statement that the strengths of the “dropout” signature is strong enough to provide a unique redshift assignment. Conversely, about 50% (i.e. 29 out of 54) of the galaxies with  $3.5 \leq z_{\text{phot}} \leq 4.5$  fall

within the M98 area (we include also the two objects at the left of the M98 area).

- Of the remaining fraction (25 out of 54) of the  $3.5 < z_{phot} \leq 4.5$  candidates, most are distributed in a “belt” around the M98 area, that is indeed occupied by high  $z$  theoretical models (see Fig. 5 of M98) but was excluded to minimize the contamination by lower redshift interlopers.

- finally, other objects lay progressively apart from the M98 region, filling the bridge toward the color position of galaxies at  $z > 4.5$ , with progressively larger  $V_{606} - I_{814}$  and smaller  $B_{450} - V_{606}$  with respect to what is required by the M98 approach. These “ $z = 4$  outliers” are typically faint in  $V_{606}$  and have a very large  $V_{606} - I_{814} \geq 1$ .

The brightest among these “ $z = 4$ -outliers” is HDF-N-3259-652, that is marked by a large circle in fig 8 and whose spectral distribution and best fitting spectrum is shown in fig 9. This object has a large  $B_{450} - V_{606}$  because it is undetected in  $B_{450}$  and is the brightest object among this class (these objects are undetected in  $B_{450}$ , so that the  $B_{450} - V_{606}$  should be read as lower limits), and has a spectroscopic redshift of 4.58 and a photometric redshift  $z = 4.26$ . It is fitted by the spectrum of a star-forming galaxy with a significant amount of dust ( $E(B - V) \simeq 0.15$  with an SMC extinction law) to account for the large  $B_{450} - V_{606}$  and  $V_{606} - I_{814}$  observed colors. As can be seen from fig 9, the unique identification of this galaxy is made possible by the additional constraints provided by the IR bands: the best-fitting solution when the J, H and Ks band are not used corresponds indeed to an evolved galaxy at  $z_{phot} = 0.57$ , consistent with the M98 plot (as for all the objects in the spectroscopic sample, the photometric redshift does not depend on how non-detection in the B band is treated).

To evaluate the effect of the IR bands on the photometric redshift selection of high  $z$  galaxies, and in particular on these “ $z=4$  outliers”, we have obtained a fit on the HDF-N and HDF-S samples after removal of the IR bands. The comparison between the 7-bands and the 4-bands photometric redshifts is shown in fig 10. It is shown that, while all the objects selected with the M98 criteria are assigned at  $3.5 < z < 4.5$  also with only 4 optical bands, a substantial number of the “ $z = 4$  outliers” is placed at  $z \leq 1.5$  when the IR bands are removed. These objects have redshifts  $z > 4$ , and are typically fitted with significant amounts of dust [ $< E(B - V) > \simeq 0.1$ ]. In all these cases the role of IR bands is to constrain the fit to relatively small values of  $I_{814} - K$ , even in the cases where only upper limits exist in the IR, with the result of discarding models of evolved or dusty galaxies at lower  $z$  that could easily mimic the red  $B_{450} - V_{606}$  and  $V_{606} - I_{814}$  optical colors.

Also the “ $z = 4$  outliers” that are placed at  $z > 4$  irrespective of the inclusion of IR bands (a total of 6 out of 54) are selected among models with  $< E(B - V) > \simeq 0.1$ , that were present also in the M98 synthetic grid but not included in the selection criteria. Respect to the M98 approach, the faint objects with large  $V_{606} - I_{814} > 1$  and  $B_{450} - V_{606} \leq 2$  were also discarded by not only because of their colors but also because they fade beyond the  $V_{606} \leq 27.7$  limit applied by M98.

Not suprisingly, the situation is different in our ground-based images. If we remove the IR bands from the NTTDF sample, all the  $z > 3.5$  candidate are found as well, and

all the  $z \simeq 4$  candidates by G98 are found by photometric redshifts, and viceversa. The reason lays in the different spectral sampling of the two filter sets. The spectral region covered by the three filters  $B_{450}$ ,  $V_{606}$  and  $I_{814}$ , where Lyman $\alpha$  blanketing starts to affect the HDF filter set already at  $z \simeq 3.5$ , is sampled by 4 different filters ( $BVrI$ ) in the ground based observations used here or by other groups.

*Summarizing, the  $3.5 < z < 4.5$  candidates that are selected with photometric redshifts in the HDFN+S data set and that lay far from the M98 region are typically predicted to be objects at  $z > 4$  with substantial amount of dust, i.e. a class of objects which multicolor criteria are biased against.* The IR bands are often required with the HDF filter set to include these objects in the sample. A correction of similar amplitude to the M98 criteria for dusty objects has been derived by Steidel et al 1999 using the observed color distribution of galaxies in their spectroscopic survey at  $z \simeq 3$ .

*It is also worth emphasizing that the differences between the methods have not been tested with spectroscopic follow-up in a systematic way.* It is certainly reassuring that HDF-N-3259-652, that lays outside the M98 area albeit it is at  $z = 4.58$ , is recovered with the photometric redshift analysis, but the major differences arise from the fainter sample, where the constraints from the IR bands are less stringent and the noise on the observed magnitudes is larger.

Another issue that should not be underestimated concerns the differences among different algorithms used for source detection and measure, even on the same data. Based on the same set of HDF-N and HDF-S images, Casertano et al 2000 find a larger number of  $z \simeq 4$  candidates than are found in the Stony Brook catalogs, at the same magnitudes and adopting the same M98 criteria, and find that the HDF-N shows less candidates respect to the HDF-S, contrary again to what it is found in the Stony Brook catalogs.

We conclude with a comment on fig 10: we note that, as expected, the lack of IR bands causes a relatively large scatter in the  $1 < z < 2$  region, the region where the major spectral breaks fall in the IR bands. However, the number of completely discrepant redshifts ( $\Delta z > 1$ ) is limited. To some extent, this reflects the fact that for a typical object the S/N ratio of the WFPC bands is always much higher than that of the IR bands, so that they dominate the  $\chi^2$  even when the IR bands are included.

## 5.2. Galaxies at $z > 4.5$

It is well known that Galactic stars are one of the main sources of foreground interlopers that may be identified as high redshift galaxies. As discussed in sect. 2.3, we have applied a pure morphological criterium to select bright stars in the HDF-S and in the NTTDF, where spectroscopic follow-up is still lacking. It is interesting to note that 8 (out of 32) of these “morphological” stars are assigned at  $z > 4$  by our photometric redshift code (see also Lanzetta 2000). Most of these objects are very bright ( $I_{AB} \leq 23.5$ ) so that the morphological classification is expected to be very robust, since high redshift galaxies are compact but resolved in high quality images, as shown by Giallisco et al 1996 and Giallisco et al 2000. However, we have complemented the morphological selection



with a comparison with the stellar library by Pickles 1998, that we have used as input to our photometric redshift code. We have therefore compared the  $\chi_{star}^2$  obtained for each object in the HDF-S with the use of the Pickles 1998 library with the  $\chi_{G1SSSEL}^2$  obtained by the ordinary procedure.

We find that, while all bright galaxies are very poorly fitted by any stellar template, with  $\chi_{star}^2 \gg \chi_{G1SSSEL}^2$  (typically by a factor of 100), 85% of the stars selected by morphological criteria have  $\chi_{star}^2 \simeq \chi_{G1SSSEL}^2$  and, in particular, five of the  $z > 4$  candidates have  $\chi_{star}^2 < \chi_{G1SSSEL}^2$ . Two typical examples are shown in fig 11. It is shown that the high redshift identification comes from the flat continuum at long wavelengths, coupled with the large spectral break in the bluer bands - all features typical of high redshift galaxies (see previous section). However, they are better fitted by an M star spectral template because of the relatively gentle fading - when compared to the abrupt drop due to the IGM at  $z > 4.5$  - at blue wavelengths and the negative slope at  $\lambda > 10000\text{\AA}$  that are both typical of M stars. We conclude that also the color properties of these objects support the morphological classification of faint halo stars.

It is important to emphasize that, once bright M-stars (i.e. objects that correspond to the morphological criteria discussed above) are removed, *no other convincing candidate at  $z > 5$  is found in the HDF-S sample.* In addition to the photometric redshift predictions, this can be tested directly by looking at the multicolor data: no object in the Stony Brook catalog of the HDF-S is detected in  $I_{F814W}$  (at  $I_{F814W} \leq 27.5$ ) but not in  $V_{F606W}$ , contrary to what is observed in the objects detected so far at  $z \geq 5$  in the HDF-N (Lanzetta et al 1996, Spinrad et al 1998). As a result, the UV luminosity density  $\phi_{1400}$  at  $z \geq 4.5$  is still poorly determined, since it changes by a factor of  $\simeq 6$  between the HDF-N and the HDF-S at  $z \geq 4.5$  (Fontana et al 1999b).

## 6. SUMMARY

This paper presents the photometric redshift catalogs that have been used in previous papers to investigate different aspects of the evolution of galaxies in the high redshift Universe, such as the history of the UV luminosity density and the number of massive galaxies already assembled at early epochs (Fontana et al 1999b) and the evolution of galaxy sizes (Poli et al 1999, Giallongo et al 2000).

A new deep multicolor (UBVrIJKs) photometric catalog has been produced of the galaxies in the NTT Deep Field and in the slightly overlapping field centered on the  $z_{em} = 4.7$  quasar BR1202-07. This has been obtained by combining the existing BVrI and JKs images with new, deep, U band observations of both fields acquired with NTT-SUSI2.

We have further presented in this paper the photometric redshift catalog drawn from this galaxy sample, using a  $\chi^2$  minimization technique based on the Bruzual and Charlot

spectral library, with the addition of dust and intergalactic absorption. We have also presented the results of applying the same photometric redshift technique to public catalogs of the HDF-N and HDF-S, where a similar optical-infrared coverage is available.

The method has been tested on a set of 125 galaxies with known spectroscopic redshifts in the HDF-N, HDF-S and AXAF fields, with a resulting accuracy  $\sigma_z \sim 0.08(0.3)$  in the redshift intervals  $z = 0 - 1.5(1.5 - 3.5)$ .

The global redshift distribution of I-selected galaxies shows a distinct peak at intermediate redshifts,  $z \simeq 0.6$  at  $I_{AB} \leq 26$  and  $z \simeq 0.8$  at  $I_{AB} \leq 27.5$  followed by a tail extending to  $z \simeq 6$ . Systematic differences exist amongst the fields, most notably the HDF-S contains a much smaller number of galaxies at  $z \simeq 0.9$  and at  $z \geq 4.5$  than the HDF-N. We have also presented the redshift distribution of the total IR-selected sample, which may be useful to tailor the planned surveys with IR spectrographs at large telescopes that will target the redshift range  $1.3 \leq z \leq 2$ . We find that the number density of galaxies in the redshift range is  $\simeq 0.15 \text{arcmin}^{-2}$  at  $J \leq 21$  and  $\simeq 1.3 \text{arcmin}^{-2}$  at  $J \leq 22$ .

We have also discussed the different results from applying color selection criteria and photometric redshifts for detecting galaxies in the redshift range  $3.5 \leq z \leq 4.5$  using the HDFs data sets. We find that photometric redshifts predict a two times larger number of high  $z$  candidates in both the HDF-N and HDF-S and show that this is primarily due to the inclusion of slightly dusty ( $E(B - V) \simeq 0.1$  with SMC extinction law) models that were discarded in the original color selection criteria conservatively applied by Madau et al 1998. In several cases, the selection of these objects is made possible by the additional constraints from the IR bands. This effect partially reflect the poor spectral sampling of the HDF filter set, and is not present in ground-based observations where a  $R - I \leq 0.5$  color selection criteria may be applied.

Finally, we show that galactic M stars may mimic  $z > 5$  candidates in the HDF filter set and that the 4 brightest candidates at  $z > 5$  in the HDF-S are, indeed, most likely to be M stars. The estimates of the UV luminosity density  $\phi_{1400}$  at  $z \geq 4.5$  from these data, when the selection against halo stars is applied, show that  $\phi_{1400}$  changes by a factor of  $\simeq 6$  between the HDF-N and the HDF-S (Fontana et al 1999b).

## Acknowledgments

The paper is based on observations made with: the ESO New Technology Telescope at the La Silla Observatory (some under the EIS programs 59.A-9005(A), 60.A-9005(A)), the NASA/ESA Hubble Space Telescope and the Kitt Peak National Observatory. The ultraviolet observations of the NTTDF were performed in SUSI-2 guaranteed time of the Observatory of Rome in the framework of the ESO-Rome Observatory agreement for this instrument.

## REFERENCES

Arnouts, S., Cristiani, S., Moscardini, L., Matarrese, S., Lucchin, F., Fontana, A., Giallongo, E., 1999a, 310, 540

Arnouts, D'Odorico, S., Cristiani, S., Zaggia, S., Fontana, A., Giallongo, E., 1999b, A&A 341, 641  
Baum, W.A., 1962, IAU Symp 15, 390

- Benitez, N., 1999 ApJ subm., astro-ph/9811189
- Bertin, E., Arnouts, S. 1996, A&AS, 117, 393
- Burstein, D., Heiles, C., 1982, AJ, 87, 1165
- Calzetti, D. 1997, in "The Ultraviolet Universe at Low and High Redshift", astro-ph/9706121
- Casertano et al, 2000, in preparation
- Cohen, J., Hogg, D., Blandford, R., Cowie, L., Hu, E., Songaila, A., Shopbell, P., Richberg, K., 2000, ApJ in press, astro-ph/9912048
- Coleman, G. D., Wu, C.-C., & Weedman, D. W. 1980, ApJS, 43, 393
- Connolly, A. J., Szalay, A. S., Dickinson, M., SubbaRao, M. U., & Brunner, R. J. 1997, ApJ, 486, L11
- Cristiani, S., Appenzeller, I., Arnouts, S., Nonino, M., Aragón-Salamanca, A., Benoist, C., da Costa, L., Dennefeld, M., Rengelink, R., Renzini, A., Szeifert, T., White, S., 2000, A&A in press, astro-ph/0004213
- Csabai, I., Connolly, A. J., Szalay, A. S., Budavari, T., 2000, AJ in press, astro-ph/9910389
- Cuby, J. G., Saracco, P., Moorwood, A. F. M., D'Odorico, S., Lidman, C., Comerón, F., Spyromilio, J., 1999, A&A, 349, L41
- Da Costa, L. et al , 1998, A&A subm. astro-ph/9812105
- Dickinson, M., 1998, in *The Hubble Deep Field*, eds. M. Livio, S. M. Fall and P. Madau (Cambridge: Cambridge University Press), P. 219
- Ellis, R. S. 1997, ARAA, 35, 389
- Fernandez-Soto, A., Lanzetta, K. M., Yahil, A., 1999, ApJ 513, 34
- Fontana, A., Cristiani, S., D'Odorico, S., Giallongo, E., Savaglio, S. 1996, MNRAS, 279, L27
- Fontana, A., D'Odorico, S., Giallongo, E., Cristiani, C., Monnet, G., AJ 1998, 115, 1225
- Fontana A., D'Odorico S., Fosbury, R., Giallongo, E., Hook, I., Poli, F., Renzini, A., Viezzer R., , 1999a, A&A 343, L19
- Fontana, A., Menci, N., D'Odorico, S., Giallongo, E., Poli, F., Cristiani, S., Moorwood, A., Saracco, P., 1999b, MNRAS, 310 L27
- Giallongo, E., D'Odorico, S., Fontana, A., Cristiani, S., Egami, E., Hu, E., McMahon, R. G., 1998, AJ 115, 2169 (G98)
- Giallongo, E., Menci, N., Poli, F., D'Odorico, S., Fontana, A., 2000, ApJ 530, L73
- Giavalisco, M., Steidel, C.C., Macchetto, F. D., 1996, ApJ, 470, 189
- Hu, E. M., McMahon, R. G. 1996, Nature, 382, 231
- Kennicutt, R. C., Tamblyn, P., & Congdon, C. W. 1994, ApJ, 435, 22
- Koo, D. C., 1985, AJ, 90, 418
- Koo, D. C. and Kron, R. G., 1992, ARA&A 30, 613
- Kron, R. G., 1980, ApJS, 43, 305
- Lanzetta, K. M., Yahil, A., Fernandez-Soto, A., 1996, Nature, 386, 759
- Lanzetta, K. M., Chen, H., , Fernandez-Soto, A., Pascarelle, S., Yahata, N., Yahil, A., 2000, in "The Hy-Redshift Universe: galaxy Formation and Evolution at High Redshift", eds Bunker, A and van Breugel, W., J., M., astro-ph/9910554
- Madau, P., 1995, ApJ, 441, 18
- Madau, P., Ferguson, H.C, Dickinson, M.E. , Giavalisco, M., Steidel, C.C., Fruchter, A., 1996, MNRAS, 283, 1388
- Madau, P., Pozzetti, L., Dickinson, M., 1998, ApJ, 498, 106
- Moorwood, A., Cuby, J. G., Lidman, C., 1998a, The Messenger, 91, 9
- Moorwood, A., Cuby, J. G., Devillard, N., Lidman, C., Saracco, P., 1998b, [http://www.hq.eso.org/science/sofi\\_deep/](http://www.hq.eso.org/science/sofi_deep/)
- Pascarelle, S. M., Lanzetta, K. M., Fernandez-Soto, A., 1998, ApJ, 501, L1
- Pei, Y.C., 1992, ApJ, 395, 130
- Pello, R., Kneib, J. P., Le Borgne, J. F., Bezecourt, J., Ebbels, T. M., Tijera, I., Bruzual, G., Miralles, J. M., Smail, I., Soucail, G., Bridges, T. J., 1999, A&A 346, 359
- Pickles, A. J., 1998, PASP, 110, 863
- Pei, Y. C. 1992, ApJ, 395, 130
- Petitjean, P., Pécontal, E. Valls-Gabaud, D., Charlot, S. 1996, Nature, 380, 411
- Pettini, M., Steidel, C. C., Adelberger, K. L., Kellogg, M., Dickinson, M., Giavalisco, M., 1997, in 'Cosmic Origins: Evolution of galaxies, stars, planet and life', Shull, Woodward and Thronson eds., ASP series
- Poli, F., Giallongo, E., Menci, N., D'Odorico, S., Fontana, 1999, ApJ, 527, 662
- Rengelink, R et al, 1998, A&A subm, astro-ph/9812190
- Saracco, P., D'Odorico, S., Moorwood, A., Buzzoni, A., Cuby, J.-G., Lidman, C. 1999, A&A, 349, 751
- Sawicki, M.J., Lin, H., Yee, H.K.C. 1997, AJ, 113, 1
- Smail, I., Hogg, D. W., Yan, L., Cohen, J. G. 1995, ApJ, 449, L105
- Spinrad, H., Stern, D., Bunker, A., Dey, A., Lanzetta, K. Yahil, A., Pascarelle, S., Fernandez-Soto, A., 1998, AJ, 116, 2617
- Steidel, C. C., Pettini, M., Hamilton, D., 1995, AJ, 110, 2519
- Steidel, C. C., Giavalisco, M., Pettini, M., Dickinson, M., Adelberger, K. L. 1996, ApJ, 462, L17
- Steidel, C. C., M., Adelberger, K. L., Giavalisco, M., Dickinson, Pettini, M., 1999, ApJ 519, 1
- Tyson, J. A., 1988, AJ 96, 1
- Wang, Y., Bahcall, N., Turner, E. L., 1998, AJ, 116, 2081
- Williams, R. E. et al. 1996, AJ, 112, 1335

TABLE 1  
SUMMARY OF THE OBSERVATIONAL DATA<sup>1</sup>

Field name	Size (arcmin <sup>2</sup> )	Magnitude limit <sup>2</sup>							
		U	B	V	Gunn r	I	J	H	K
BR1202	4	26.9	26.5	26	25.6	25	23.4	–	21.7
NTTDF	4.8	26.9	27.5	26.85	26.5	26.4	23.4	–	21.7
HDF-N	4.2	28.4 <sup>3</sup>	29.2 <sup>3</sup>	29.5 <sup>3</sup>		29 <sup>3</sup>	23.8	22.9	22.4
HDF-S	3.9	28.2 <sup>3</sup>	29 <sup>3</sup>	29.3 <sup>3</sup>		28.7 <sup>3</sup>	24	22.1	22

<sup>1</sup>: Note on the photometric system adopted: *U*, F300W, F450W, F606W and F814W are in AB system: all other data are in the Johnson (i.e. Vega zeropointed) system.  $J_{AB}$ ,  $H_{AB}$ , and  $K_{AB}$  magnitudes in the HDF catalogs have been converted to Johnson applying  $J = J_{AB} - 0.87$ ,  $H = H_{AB} - 1.34$  and  $K = K_{AB} - 1.84$ .

<sup>2</sup>: at  $3\sigma$ . Limiting magnitudes have been estimated from the photometric catalogs used in the paper, and defined as the typical value at which  $\Delta m = 1.08/3$ . Only exceptions are the F606W and F814W bands, that have been taken with the same criteria from the STScI public catalogs.

<sup>3</sup>: The F300W, F450W, F606W and F814W filters of WFPC2 were used for the optical observations, and magnitudes are given in the AB system

TABLE 2  
NTTDF AND BR1202 PHOTOMETRIC CATALOGS<sup>1</sup>

ID <sup>2</sup>	$\alpha$ [h]	$\delta$ [deg]	$U_{AB}$	B	V	R	I	J	K	$z_{phot}$	$r_{hl}$ <sup>3</sup>
n0001	12:05:18.01	-7:44:40.98	24.74	24.28	23.33	22.85	22.63	21.92	21.01	0.34	0.25
n0002	12:05:18.43	-7:44:40.43	24.72	24.46	23.83	23.06	22.12	20.93	19.43	0.80	0.63
n0003	12:05:18.21	-7:44:39.53	23.35	23.20	22.42	21.79	21.61	21.14	20.28	0.26	0.66
n0005	12:05:17.81	-7:43:33.34	25.19	24.86	24.27	23.96	23.54	22.28	21.76	0.10	
n0006	12:05:17.79	-7:43:26.36	25.80	25.88	24.43	24.12	23.97	22.49	21.63	0.29	

<sup>1</sup>The

complete version of this table is in the electronic edition of the Journal. The printed edition contains only a sample.

<sup>2</sup>Objects named *n0001*, *n0002* etc, refer to the NTTDF; objects named *q0001*, *q0002* refer to objects in the QSO field (BR1202).

<sup>3</sup>Half-light radius, as measured in Poli et al 1999.

TABLE 3

TOTAL NUMBER AND SURFACE DENSITIES OF GALAXIES AT  $z \geq 1$  IN THE NTTDF + HDF<sup>-</sup> + HDF-S SAMPLE AS A FUNCTION OF REDSHIFT. NUMBERS WITHIN BRACKETS REFER TO THE INDIVIDUAL FIELDS, NAMELY NTTDF (UPPER), HDF-N (MIDDLE) AND HDF-S (LOWER).

$z$	gal	gal/arcmin <sup>2</sup>	gal	gal/arcmin <sup>2</sup>	gal	gal/arcmin <sup>2</sup>			
	$J \leq 20$		$J \leq 21$		$J \leq 22$				
<i>all</i>	43	$\begin{pmatrix} 16 \\ 16 \\ 11 \end{pmatrix}$	3.08	96	$\begin{pmatrix} 32 \\ 36 \\ 28 \end{pmatrix}$	6.88	196	$\begin{pmatrix} 68 \\ 74 \\ 54 \end{pmatrix}$	14.06
$1 < z \leq 1.25$	1	$\begin{pmatrix} 0 \\ 1 \\ 0 \end{pmatrix}$	0.07	12	$\begin{pmatrix} 1 \\ 7 \\ 4 \end{pmatrix}$	0.86	38	$\begin{pmatrix} 11 \\ 16 \\ 11 \end{pmatrix}$	2.73
$1.25 < z \leq 1.5$	0	$\begin{pmatrix} 0 \\ 0 \\ 0 \end{pmatrix}$	0.	1	$\begin{pmatrix} 0 \\ 0 \\ 1 \end{pmatrix}$	0.07	13	$\begin{pmatrix} 2 \\ 4 \\ 7 \end{pmatrix}$	0.93
$1.5 < z \leq 2$	1	$\begin{pmatrix} 1 \\ 0 \\ 0 \end{pmatrix}$	0.07	1	$\begin{pmatrix} 1 \\ 0 \\ 0 \end{pmatrix}$	0.07	5	$\begin{pmatrix} 2 \\ 2 \\ 1 \end{pmatrix}$	0.36
$z > 2$	0	$\begin{pmatrix} 0 \\ 0 \\ 0 \end{pmatrix}$	0	0	$\begin{pmatrix} 0 \\ 0 \\ 0 \end{pmatrix}$	0	2	$\begin{pmatrix} 1 \\ 1 \\ 0 \end{pmatrix}$	0.14
	$K_s \leq 19$		$K_s \leq 20$		$K_s \leq 21$				
<i>all</i>	69	$\begin{pmatrix} 24 \\ 28 \\ 17 \end{pmatrix}$	4.95	125	$\begin{pmatrix} 43 \\ 44 \\ 38 \end{pmatrix}$	8.98	247	$\begin{pmatrix} 85 \\ 88 \\ 74 \end{pmatrix}$	17.72
$1 < z \leq 1.25$	6	$\begin{pmatrix} 0 \\ 4 \\ 2 \end{pmatrix}$	0.43	24	$\begin{pmatrix} 5 \\ 11 \\ 8 \end{pmatrix}$	1.72	48	$\begin{pmatrix} 15 \\ 20 \\ 13 \end{pmatrix}$	3.44
$1.25 < z \leq 1.5$	1	$\begin{pmatrix} 0 \\ 0 \\ 1 \end{pmatrix}$	0.07	5	$\begin{pmatrix} 1 \\ 0 \\ 4 \end{pmatrix}$	0.36	15	$\begin{pmatrix} 2 \\ 4 \\ 9 \end{pmatrix}$	1.08
$1.5 < z \leq 2$	1	$\begin{pmatrix} 1 \\ 0 \\ 0 \end{pmatrix}$	0.07	5	$\begin{pmatrix} 1 \\ 3 \\ 1 \end{pmatrix}$	0.36	17	$\begin{pmatrix} 3 \\ 6 \\ 8 \end{pmatrix}$	1.21
$z > 2$	0	$\begin{pmatrix} 0 \\ 0 \\ 0 \end{pmatrix}$	0	0	$\begin{pmatrix} 0 \\ 0 \\ 0 \end{pmatrix}$	0	13	$\begin{pmatrix} 8 \\ 2 \\ 3 \end{pmatrix}$	0.93

FIG. 1.— THIS FIGURE IS AVAILABLE AT <http://www.mporzio.astro.it/HIGHZ>. The total field of view around BR1202-07, made by the superposition of the two NTT fields discussed here. Upper field is the BR1202 field. A square marks the position of the  $z = 4.7$  QSO. North is up, East left.

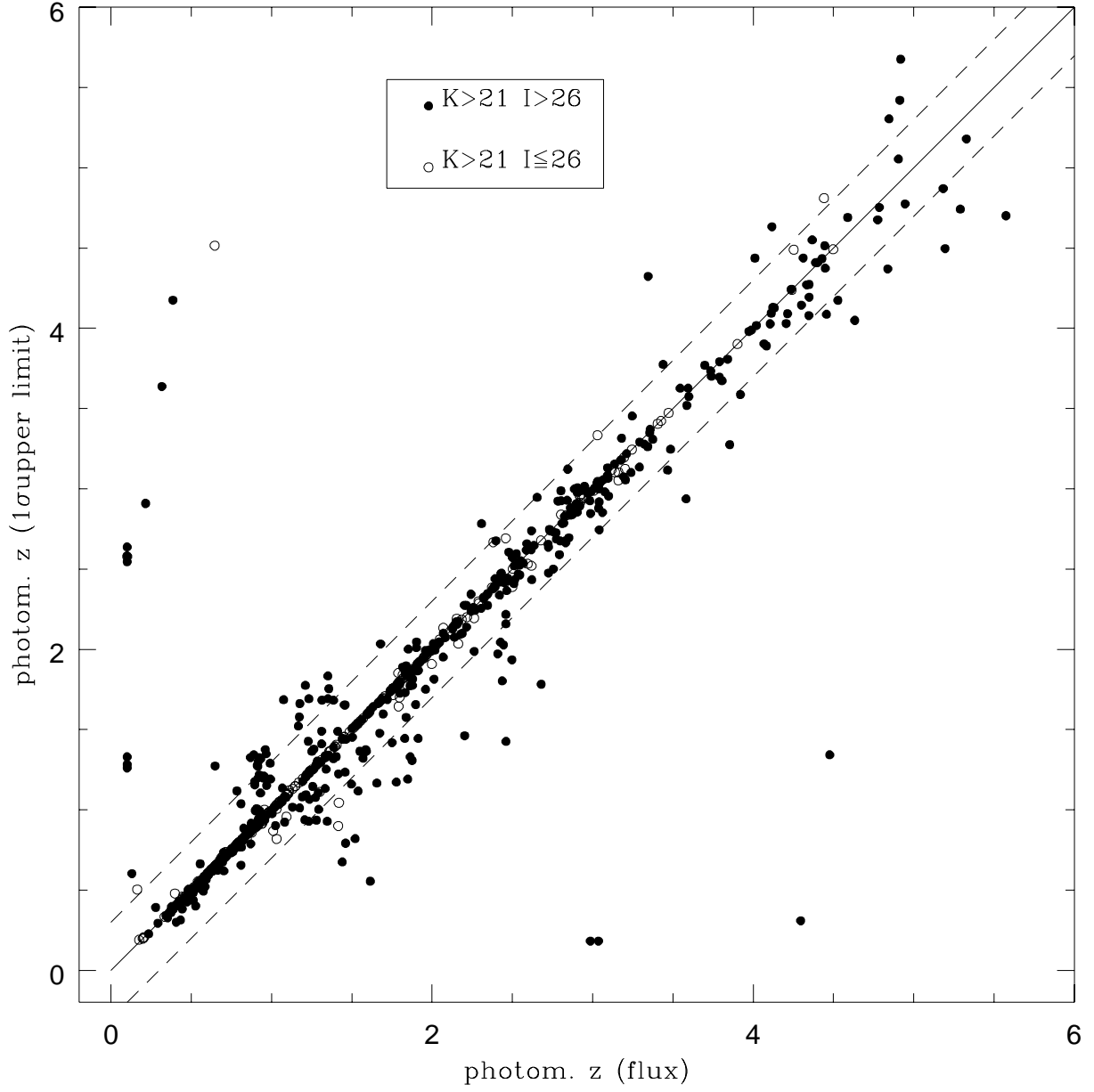


FIG. 2.— Comparison between the photometric redshifts in the HDF-N obtained with the “flux” format (on x-axis) used in the paper and with the “magnitude” format with upper limits at  $1\sigma$  level (see text for full details). The symbols for objects with different  $I_{814}$  magnitudes are given in the legend. Objects with  $K \leq 21$  are shown as crosses, but lay along the bisector line and are not visible.

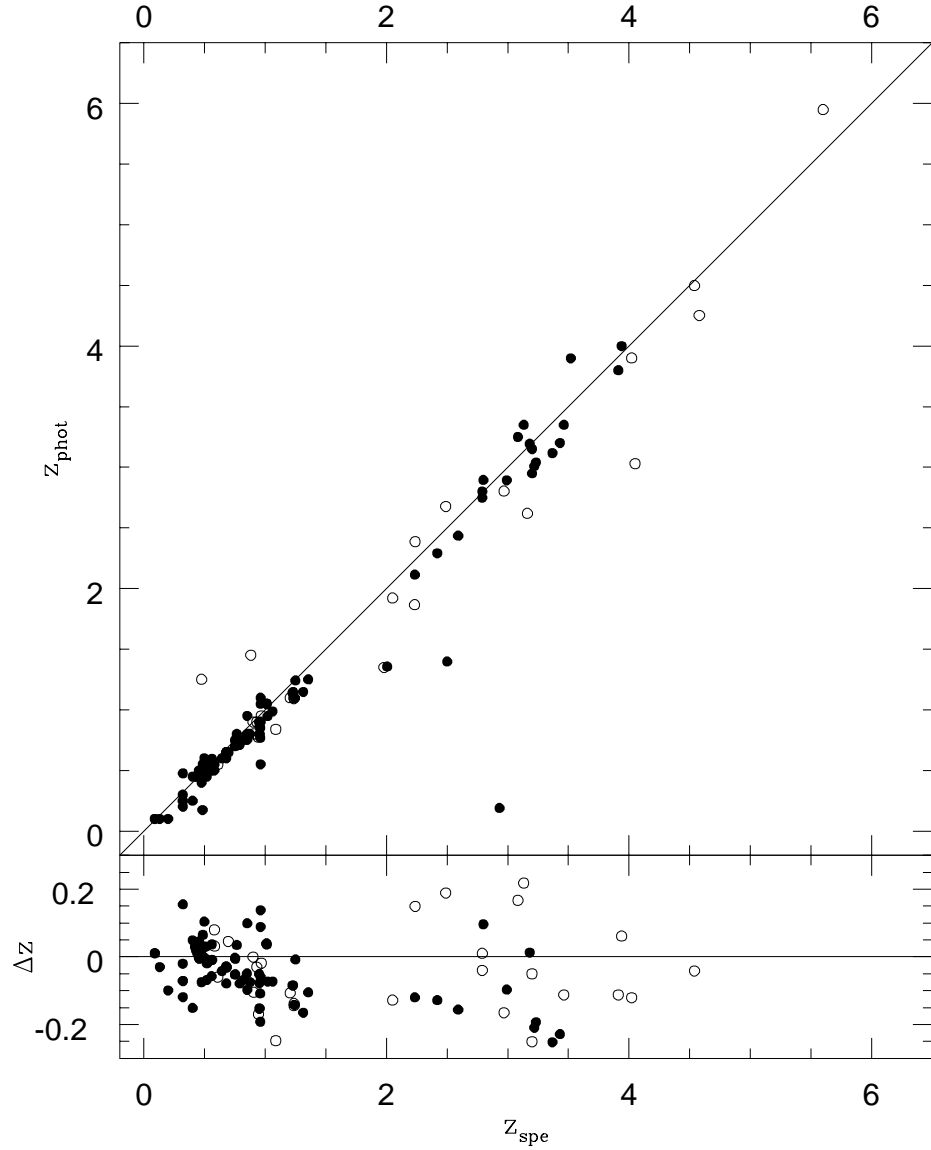


FIG. 3.— Comparison between the spectroscopic and photometric redshifts in a sample of 125 galaxies in the HDF-N, HDF-S and AXAF fields. Filled circles show objects from HDF-S, AXAF and with secure redshifts in the HDF-N (i.e. those with redshift quality class = 1,2,4 or 6 in Cohen et al 2000), while empty circles are objects with more uncertain redshift in the HDF-N.



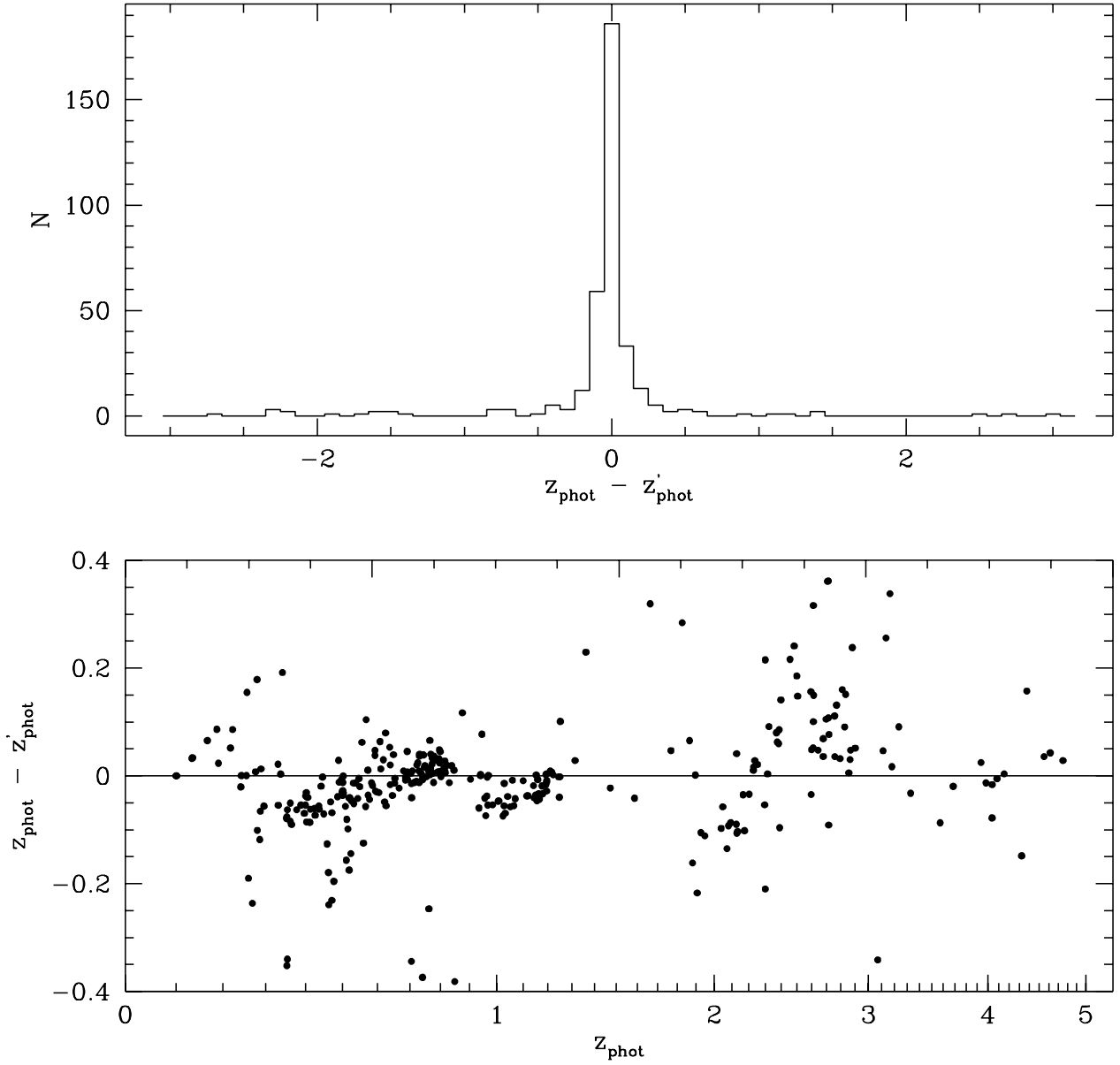


FIG. 4.— Differences in the photometric redshifts estimated on the NTTDF when the two photometric calibrations are used.  $z'_{\text{phot}}$  mark the photometric redshifts when the original calibration is used, while  $z_{\text{phot}}$  are those resulting from the adopted one. Upper panel shows the histogram of  $z_{\text{phot}} - z'_{\text{phot}}$ , while the lower one shows  $z_{\text{phot}} - z'_{\text{phot}}$  as a function of  $z_{\text{phot}}$ .

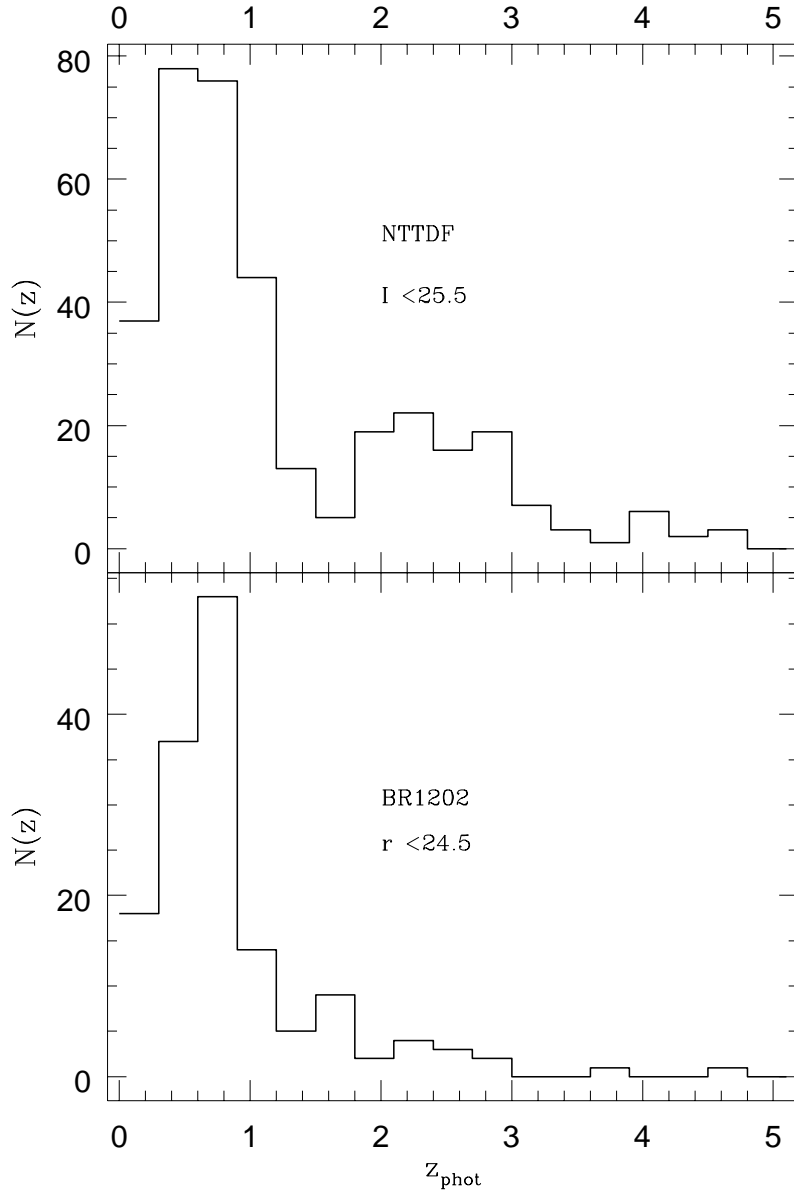


FIG. 5.— Redshift distribution in the NTT Deep Field (upper panel) and in the BR1202 field (lower). The samples are selected at different magnitude limits (see legend).

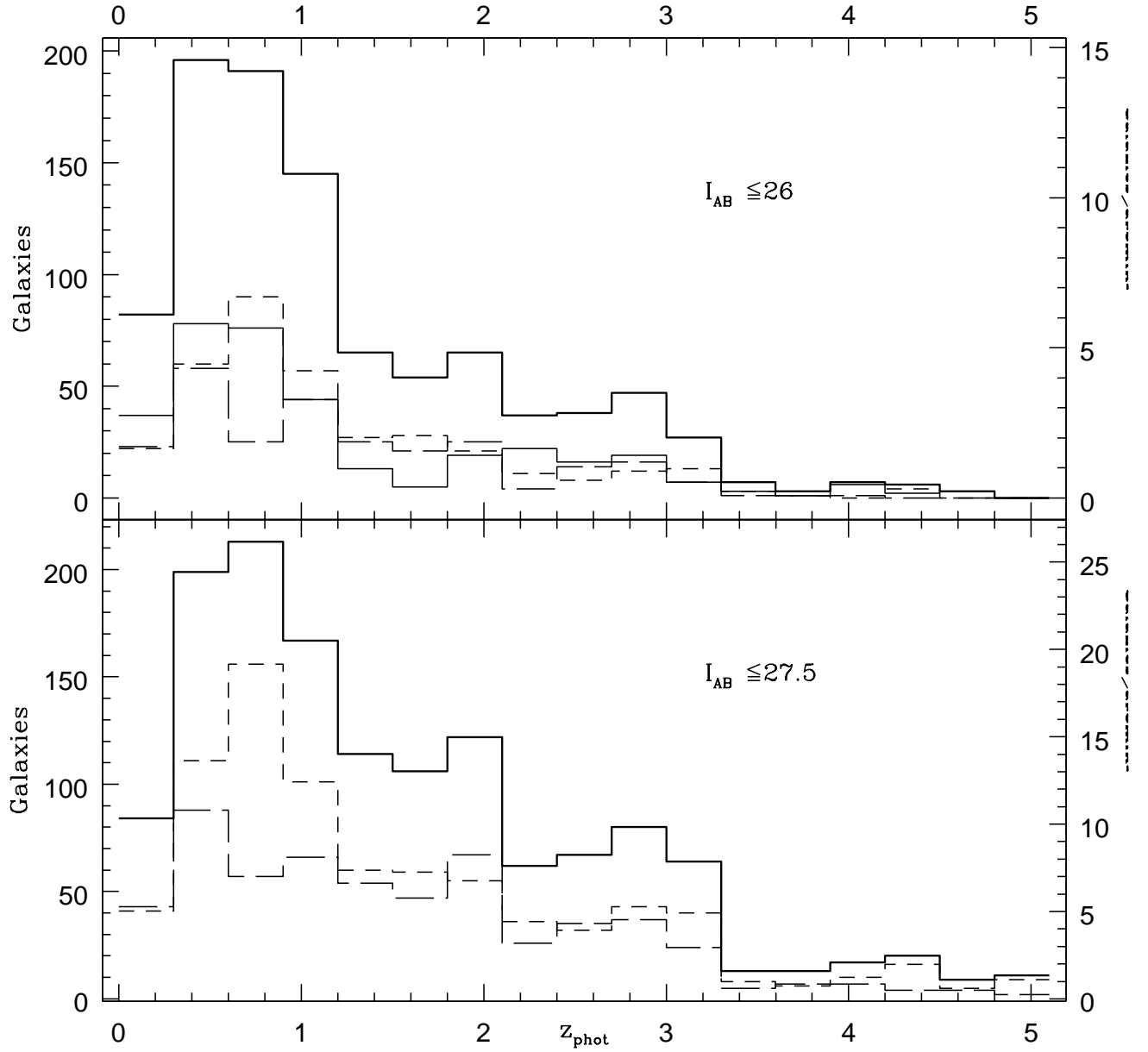


FIG. 6.— Redshift distribution in the faintest I-band selected catalogs. Thick solid line is the total redshift distribution, thin solid line is the NTTDF, dashed line is the HDF-N and long-dashed line is the HDF-S. Left y-axis shows the number of galaxies in each bin, while the right axis shows the surface density of galaxies in each bin in the total sample (thick solid curve).

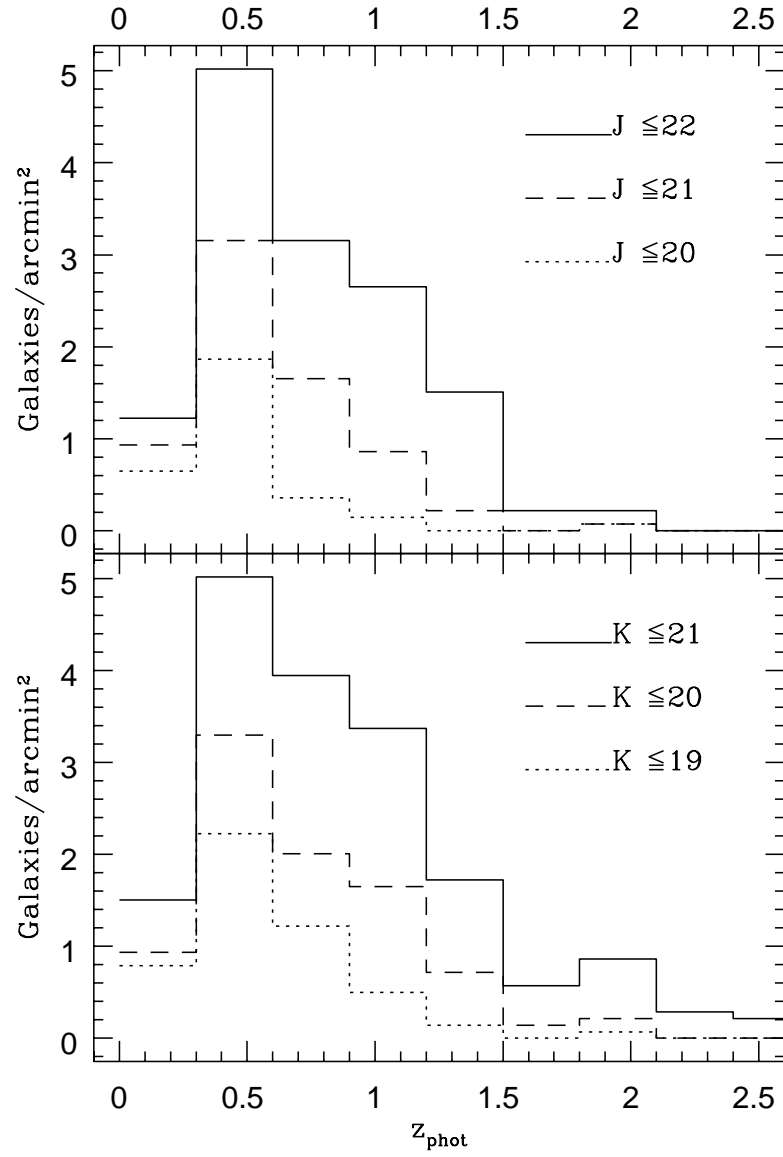


FIG. 7.— Redshift distribution in J and  $K_s$ -band selected catalogs. All curves are the sum of NNTDF, HDF-N and HDF-S. Different magnitude limits are shown in the legends.  $J_{AB}$  and  $K_{AB}$  magnitudes in the HDF catalogs have been converted to Johnson applying  $J = J_{AB} - 0.87$  and  $K = K_{AB} - 1.84$

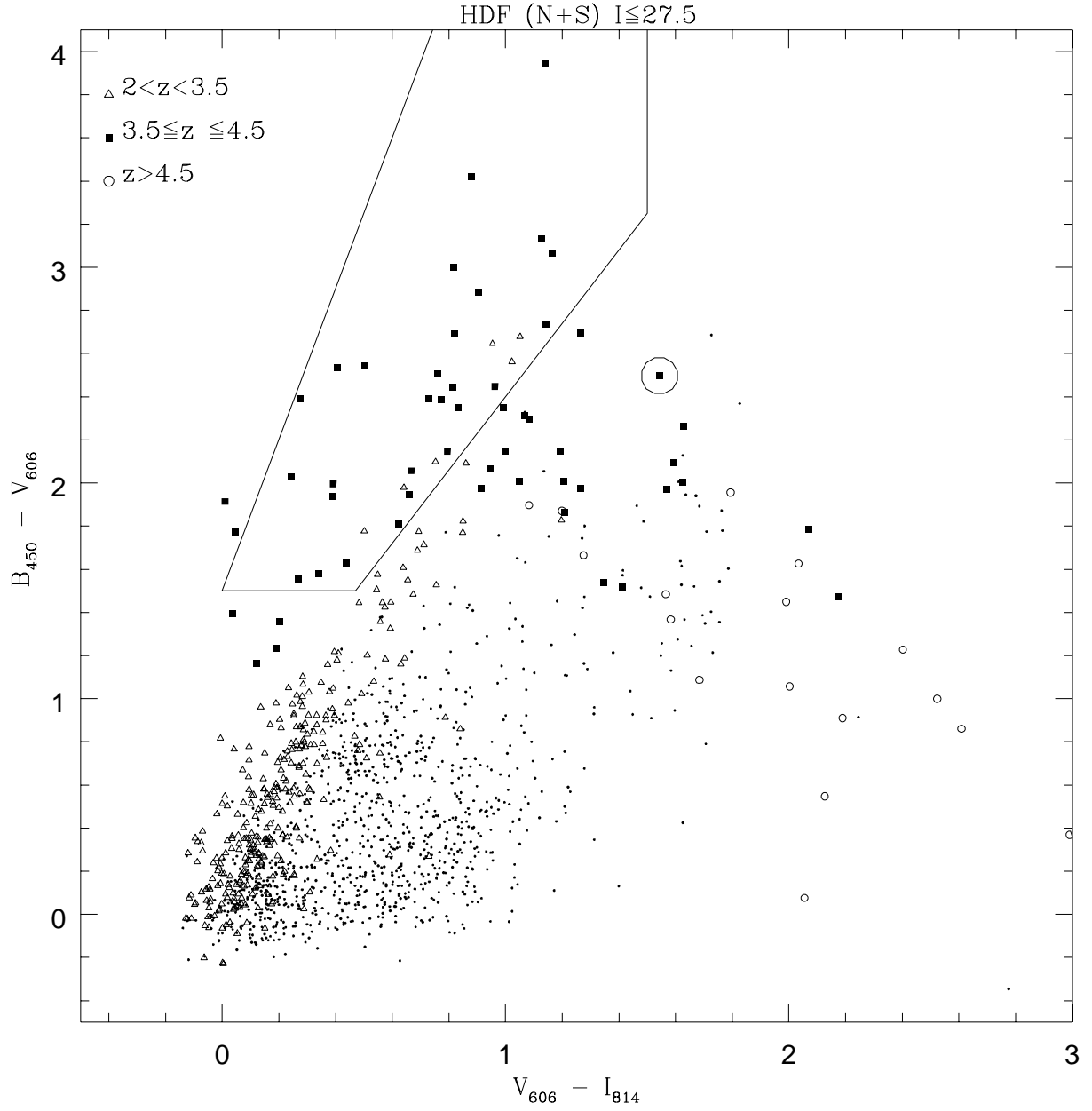


FIG. 8.— Position in the  $B_{450} - V_{606}$  vs  $V_{606} - I_{814}$  plane of the galaxies in the HDF-N and HDF-S. Galaxies at photometric redshifts  $z_{phot} \geq 2$  are shown with different symbols (see legend). Flux upper limits are computed at  $1\sigma$  level. The continuous line defines the region proposed by M98 to select galaxies in the redshift range  $3.5 \leq z \leq 4.5$ .

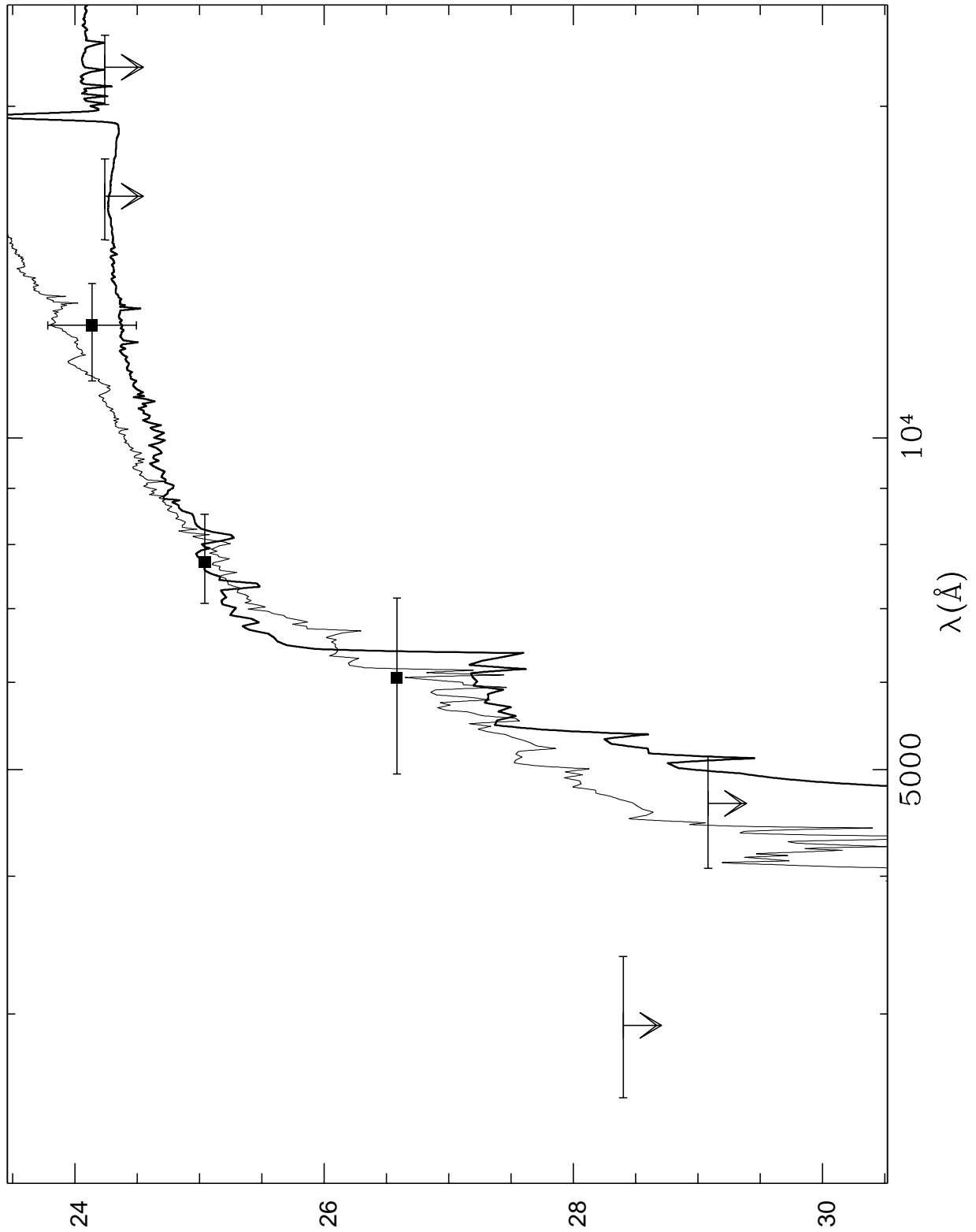


FIG. 9.— Observed spectral distribution in the HDF-N filter set and best-fitting spectra for HDF-N-3259-652, that has a spectroscopic redshift of 4.58 and is assigned a photometric redshift  $z = 4.26$ . Solid line shows the best fitting spectrum at  $z = 4.26$  when the IR bands are included, while the thin line shows the best fitting spectrum at  $z = 0.57$  when only the 4 optical bands are used.

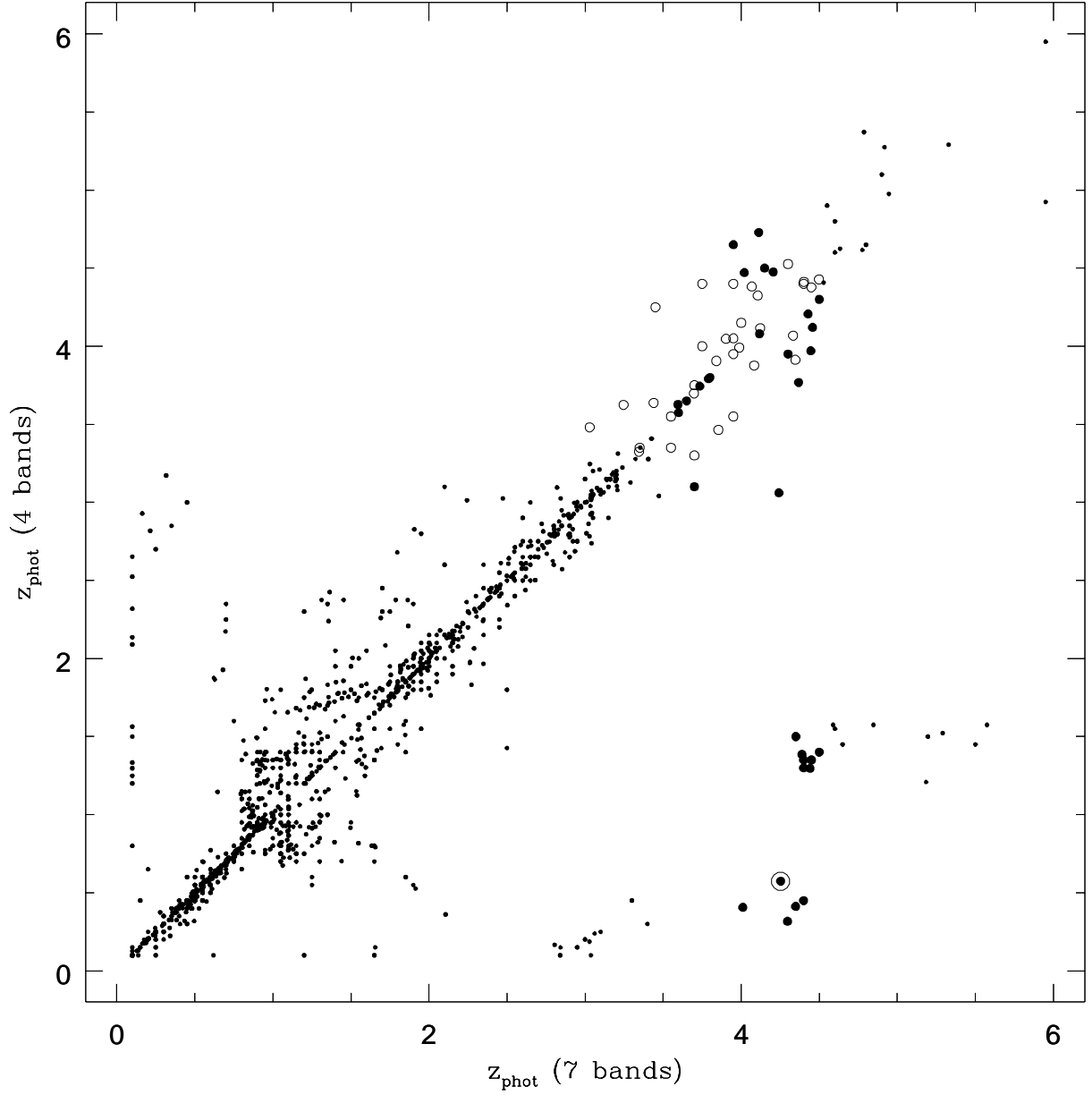


FIG. 10.— Comparison between photometric redshifts in the HDF-N with all 7 bands (x-axis) and with optical WFPC only (y-axis). Large empty dots are galaxies lying within the M98 diagram at  $3.5 < z < 4.5$ . Large filled dot are galaxies outside the M98 selection criteria that are placed at  $3.5 < z_{\text{phot}} < 4.5$  when all 7 bands are used. As in Fig. 9, HDF-N-3259-652 is marked by a large circle.

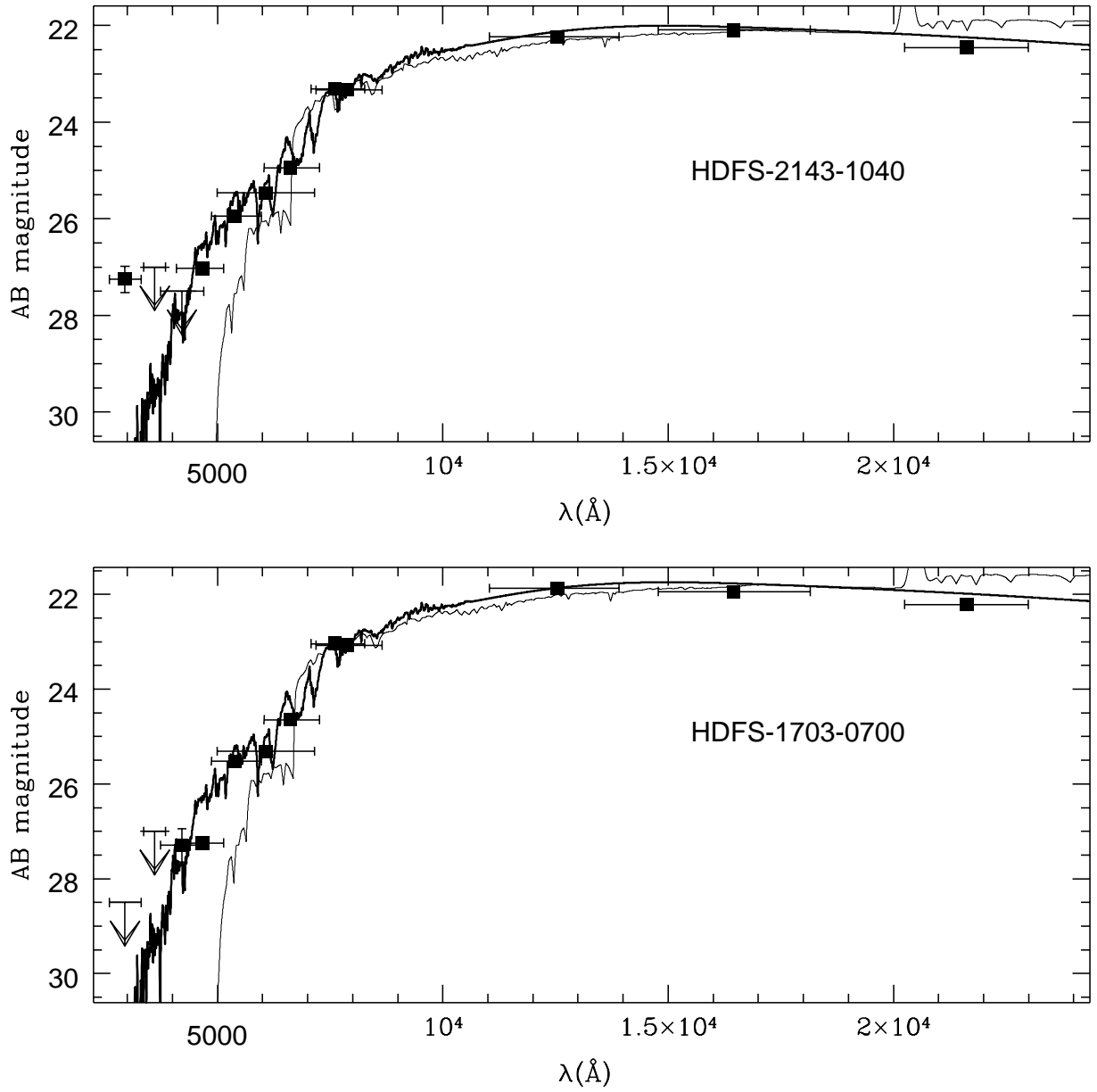


FIG. 11.— Observed spectral distribution in the HDF-S filter set and best-fitting spectra for HDF-S-2143-1040 and HDF-S-1703-0700. Thin solid line shows the best fitting spectrum at  $z \simeq 4.5$  when the IR bands are included, while the thick line shows the best fitting spectrum for an M star of the Pickles 1998 library.



TABLE 1

ID	$\alpha$ [h]	$\delta$ [deg]	U	B	V	R	I	J	K	$z_{phot}$	$r_{hl}$
n0001	12: 5:18.01	-7:44:40.98	24.74	24.28	23.33	22.85	22.63	21.92	21.01	0.34	0.25
n0002	12: 5:18.43	-7:44:40.43	24.72	24.46	23.83	23.06	22.12	20.93	19.43	0.80	0.63
n0003	12: 5:18.21	-7:44:39.53	23.35	23.20	22.42	21.79	21.61	21.14	20.28	0.26	0.66
n0005	12: 5:17.81	-7:43:33.34	25.19	24.86	24.27	23.96	23.54	22.28	21.76	0.10	-
n0006	12: 5:17.79	-7:43:26.36	25.80	25.88	24.43	24.12	23.97	22.49	21.63	0.29	-
n0007	12: 5:18.04	-7:45: 1.96	24.26	23.85	23.17	22.29	21.38	20.09	18.63	0.74	0.59
n0009	12: 5:17.99	-7:44:47.85	25.19	24.97	24.67	24.11	23.75	22.56	21.80	0.73	-
n0011	12: 5:18.09	-7:44:24.83	25.24	25.26	25.19	24.23	23.77	23.11	22.24	0.69	0.26
n0012	12: 5:18.08	-7:43:52.76	25.13	25.06	24.58	24.22	24.27	23.64	25.65	0.35	0.40
n0013	12: 5:18.15	-7:43:55.28	25.30	24.89	24.25	23.96	23.62	23.51	21.32	2.70	0.43
n0015	12: 5:18.37	-7:45: 1.21	25.85	30.05	25.90	24.17	23.92	23.73	22.13	4.15	0.36
n0016	12: 5:18.43	-7:43: 9.44	25.80	24.85	23.84	22.77	22.11	20.97	19.55	0.40	0.45
n0017	12: 5:18.33	-7:45: 5.45	25.29	25.08	24.85	24.33	24.14	23.21	22.08	0.68	0.12
n0019	12: 5:18.26	-7:43:14.77	25.82	25.43	24.66	24.28	24.01	22.41	20.94	1.88	0.44
n0020	12: 5:18.27	-7:43: 8.55	24.90	25.05	24.17	24.41	23.97	22.73	22.60	0.25	-
n0022	12: 5:18.34	-7:45:11.89	26.14	26.00	25.80	25.13	24.59	30.00	22.60	0.75	0.41
n0023	12: 5:18.38	-7:44:13.97	26.56	26.03	25.68	24.98	24.57	23.30	22.32	1.20	1.46
n0024	12: 5:18.46	-7:45: 0.38	27.49	25.92	25.42	24.89	24.51	23.36	21.98	2.30	0.32
n0026	12: 5:18.66	-7:44:16.97	24.48	24.25	23.90	23.29	22.94	21.56	20.39	1.19	0.43
n0027	12: 5:19.60	-7:43:33.46	22.15	21.26	20.08	19.30	18.85	17.79	16.65	0.25	1.11
n0029	12: 5:18.48	-7:44:25.02	26.34	27.30	26.28	25.30	24.60	23.57	23.95	0.65	0.15
n0030	12: 5:18.58	-7:43:14.03	25.17	25.10	24.36	23.84	23.18	22.23	20.76	0.77	0.47
n0032	12: 5:19.08	-7:43:24.51	23.98	23.02	21.73	20.87	20.43	19.49	18.49	0.33	0.60
n0033	12: 5:18.54	-7:44: 5.85	30.20	30.05	27.18	25.56	24.83	25.32	23.01	4.32	0.15
n0034	12: 5:18.89	-7:44:18.35	23.95	23.92	23.49	22.94	22.20	21.22	20.11	0.81	0.65
n0036	12: 5:18.60	-7:44:33.28	25.97	25.53	25.17	25.29	24.38	23.78	30.00	0.96	0.19
n0037	12: 5:18.80	-7:44: 1.86	25.29	25.20	24.95	24.46	23.92	22.85	22.29	0.80	0.48
n0039	12: 5:19.00	-7:44:54.74	24.67	24.55	24.09	23.49	23.08	21.65	20.47	1.16	0.35
n0040	12: 5:18.77	-7:45: 5.73	25.49	25.05	24.83	24.19	24.01	22.18	21.33	1.31	0.16
n0041	12: 5:18.79	-7:44:37.97	28.30	25.50	25.02	24.56	24.23	23.85	21.74	2.68	0.33
n0042	12: 5:18.64	-7:43:19.25	26.50	26.33	26.27	25.81	25.37	30.00	22.93	1.21	0.18
n0043	12: 5:19.16	-7:43:29.42	24.46	24.57	24.39	23.27	22.79	22.41	20.98	0.65	0.65
n0045	12: 5:18.73	-7:44:26.77	25.98	25.76	25.75	25.84	25.09	25.60	23.64	0.13	0.10
n0046	12: 5:18.74	-7:44: 3.03	25.87	26.32	26.14	25.26	24.34	24.20	30.00	0.80	0.19
n0047	12: 5:18.76	-7:45:13.33	30.20	28.00	26.33	25.19	25.37	23.80	24.29	4.04	0.15
n0048	12: 5:18.95	-7:45: 4.59	24.95	24.74	24.35	23.64	23.21	22.07	20.60	0.67	0.31
n0049	12: 5:19.41	-7:44:44.51	23.55	22.54	21.25	20.41	19.93	18.82	17.64	0.28	0.52
n0050	12: 5:18.80	-7:43:34.58	27.77	26.13	25.88	25.09	24.81	23.91	23.20	2.32	0.16
n0051	12: 5:18.89	-7:44:55.82	30.20	28.19	26.92	25.57	25.04	23.46	22.67	4.38	0.28
n0052	12: 5:19.39	-7:44:40.43	23.32	23.22	22.67	21.88	21.16	20.18	19.11	0.73	0.45
n0053	12: 5:19.06	-7:44: 1.89	25.19	24.52	24.18	23.83	23.57	23.16	21.30	2.39	0.39
n0054	12: 5:18.96	-7:43:36.32	27.13	25.78	25.11	24.81	24.63	23.66	23.78	2.77	0.40
n0055	12: 5:19.03	-7:43:56.78	26.07	26.37	25.50	24.37	23.30	21.56	20.08	0.76	0.01
n0056	12: 5:19.01	-7:43:53.08	25.93	25.42	25.34	24.96	24.82	23.84	22.60	2.30	0.38
n0057	12: 5:18.97	-7:43:39.89	26.81	27.32	26.75	25.45	25.18	24.01	23.26	0.62	0.15
n0058	12: 5:18.99	-7:44:21.08	30.20	28.33	26.06	25.32	24.81	24.20	22.45	3.07	0.07
n0059	12: 5:19.02	-7:45: 0.52	26.92	26.97	26.81	26.11	25.01	25.21	30.00	0.94	-
n0060	12: 5:19.01	-7:43:12.38	25.75	25.25	25.05	24.75	24.57	24.23	22.28	2.37	0.22
n0061	12: 5:19.38	-7:44:16.98	24.07	23.96	23.48	22.72	22.20	21.25	20.14	0.69	0.45
n0062	12: 5:19.13	-7:44:56.58	25.25	25.50	25.05	24.43	23.88	22.68	21.62	0.73	-
n0063	12: 5:19.14	-7:45:14.04	25.50	25.13	24.91	24.57	24.51	23.30	23.52	2.13	0.20
n0069	12: 5:19.15	-7:43:37.65	25.09	25.19	24.99	24.77	24.49	23.09	30.00	1.66	0.14
n0072	12: 5:19.20	-7:43:16.70	25.77	25.39	25.18	24.82	24.29	23.26	21.75	1.14	0.43
n0073	12: 5:19.27	-7:44: 3.11	26.21	25.62	25.15	24.89	24.75	23.73	22.78	0.10	0.34
n0074	12: 5:19.17	-7:43:42.29	27.51	27.02	25.91	25.53	25.36	24.69	30.00	3.33	0.22
n0075	12: 5:19.23	-7:43:27.87	26.08	25.61	25.36	25.24	25.28	30.00	23.02	2.60	0.30
n0076	12: 5:19.24	-7:44:19.79	26.05	25.98	25.81	25.30	24.55	23.50	22.62	1.01	0.08
n0077	12: 5:19.21	-7:44:12.05	26.47	27.65	26.50	26.00	25.10	24.41	25.63	0.70	-
n0078	12: 5:19.21	-7:43:49.86	26.08	27.18	26.27	25.02	25.10	30.00	24.13	0.74	0.99